

Buckle folding in the Northern Calcareous Alps - Field observations and numeric experiments

Sinah Kilian^{a,*}, Hugo Ortner^a, Barbara Schneider-Muntau^b

^a Institute of Geology, University of Innsbruck, Innrain 52f, 6020, Innsbruck, Austria

^b Unit of Geotechnical and Tunnel Engineering, University of Innsbruck, Technikerstraße 13, 6020, Innsbruck, Austria

ARTICLE INFO

Keywords:

Buckle folds
Décollement folds
Detachment folds
Linear elastic
Numeric modelling
Abaqus

ABSTRACT

We report the results of a numerical modelling study based on folds in the western Northern Calcareous Alps (NCA) fold-and-thrust belt. We study boundary conditions of folding based on the mechanical properties of the rocks involved. One key control on the model is stratigraphy that can be simplified to three layers: (1) an incompetent base along the décollement of the thrust sheet, and (2) an up to 3 km thick competent layer, which is overlain by (3) an incompetent top layer. The incompetent base layer needs to be very weak to facilitate folding and is a salt-bearing evaporitic unit. Another key is erosion prior to folding. It needs to remove half of the competent layer to allow the creation of folds with limb lengths comparable to field observations. The results of the numeric model contribute to the understanding of the structural development in the western NCA. Folding within the upper thrust sheet was only possible above a salt-bearing décollement and after a decrease in lithostatic pressure related to Upper Cretaceous and/or Paleogene erosion.

1. Introduction

Fold-and-thrust belts are one of the principal sources of hydrocarbons (Goffey et al., 2010; Lacombe et al., 2007; Nemcok et al., 2005), and increasingly, of hydrothermal energy. The understanding of the internal geometry is therefore a prerequisite to uncover hidden structures. Foreland fold-and-thrust belts frequently show a basal evaporitic décollement horizon, e.g., Appalachian Plateau, Pyrenees, Carpathians, Zagros Mountains (Davis and Engelder, 1985). Fold geometries within such salt-floored fold-and-thrust belts vary from the classical models (as proposed by, e.g., Suppe, 1983). The deformation style depends on the thickness and the mechanical properties of the involved layers (e.g., Davis and Engelder, 1985). A common attribute in salt-floored fold-and-thrust belts is the development of buckle folds above the décollement (e.g., Fernandez and Kaus, 2014; Humair et al., 2020; Mitra, 2002; Nilfouroushan et al., 2013; Poblet et al., 1998; Verges, 2012; Yamato et al., 2011). Buckle folds develop due to competence contrast between the basal incompetent décollement (often salt) and the competent units above. The shape of buckle folds is entirely controlled by the physical and mechanical properties of the layers (Barani, 2012; Currie et al., 1962; Davis and Engelder, 1985). It is assumed that buckled

folds maintain the initial arc length during ongoing shortening and only the amplitude increases (e.g., Price and Cosgrove, 1990; Schmalholz and Podladchikov, 2001). That means that the initial arc length is constant during ongoing shortening which in turn is the prerequisite for the comparison between folds at a different stage of shortening and between analytical and field data.

The Northern Calcareous Alps (NCA) of the eastern European Alps are a thin-skinned fold-and-thrust belt. Numerous studies (Eisbacher and Brandner, 1996; Heißel, 1978; Kilian and Ortner, 2019; Linzer et al., 1995; Tollmann, 1976b) showed that the Permian salt-bearing succession (Haselgebirge) is the basal décollement for the Karwendel thrust sheet of the western NCA. Also other thrust sheets of the NCA were separated from their former basement along this décollement (Eisbacher and Brandner, 1996; Granado et al., 2018; Linzer et al., 1995), and the role of salt tectonic processes in the eastern NCA was highlighted recently (Fernández et al., 2020; Granado et al., 2018; Strauss et al., 2021).

The focus of this study are the km-scale folds above one of the main thrusts (Karwendel thrust) in the Karwendel Mountains (Fig. 1). Our structural investigations of macroscale structures lead to the assumption that km-scale folds above the thrust are buckle folds, developed due to

* Corresponding author.

E-mail addresses: sinah.kilian@arbeitsinspektion.gv.at (S. Kilian), hugo.ortner@uibk.ac.at (H. Ortner), barbara.schneider-muntau@uibk.ac.at (B. Schneider-Muntau).

<https://doi.org/10.1016/j.jsg.2021.104416>

Received 21 October 2020; Received in revised form 25 June 2021; Accepted 30 June 2021

Available online 10 July 2021

0191-8141/© 2021 Elsevier Ltd. All rights reserved.

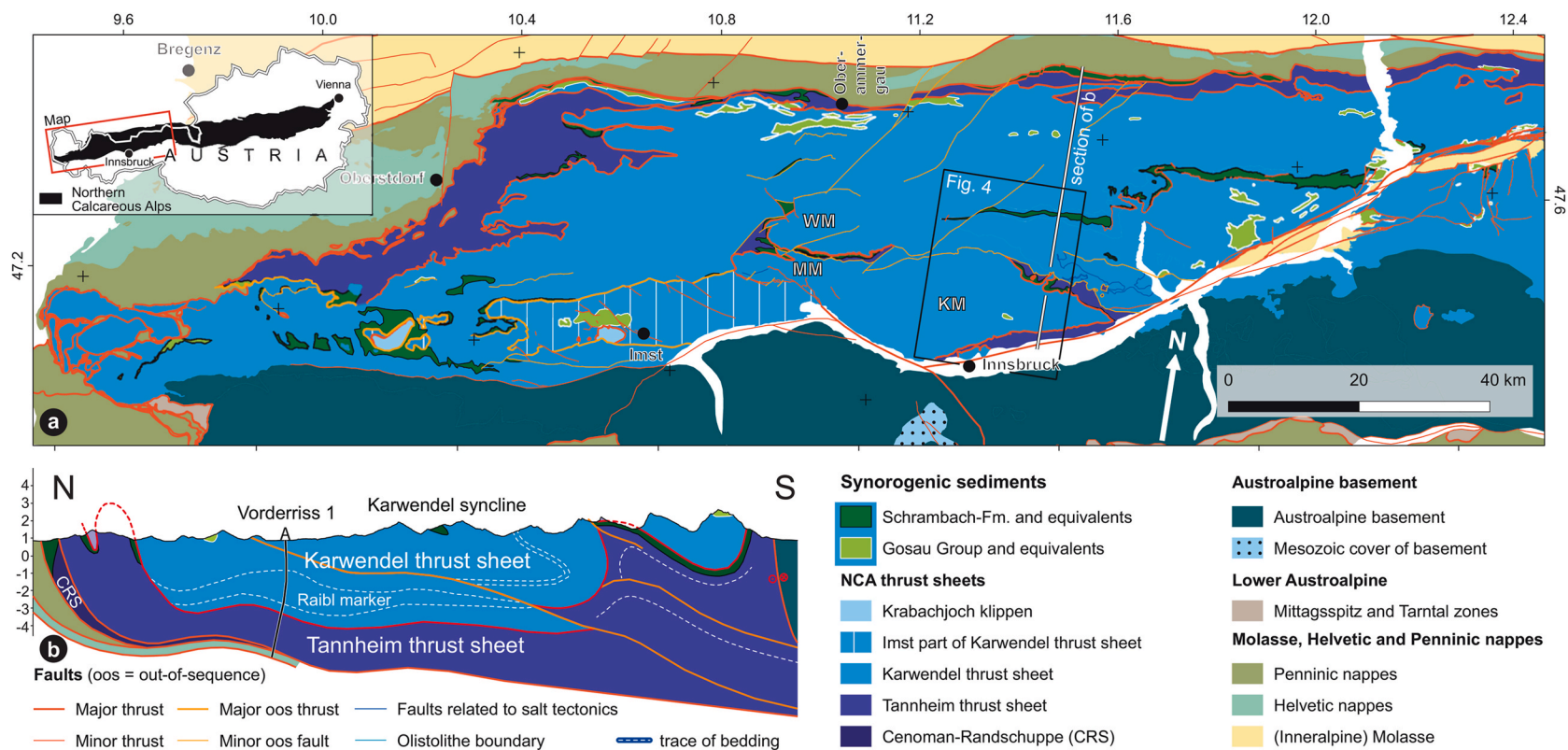


Fig. 1. Tectonic map of the western part of the Northern Calcareous Alps (modified from Ortner, 2016). WM = Wetterstein Mountains; MM = Mieming Mountains; KM = Karwendel Mountains. Inset (a): Position of the main map in the Northern Calcareous Alps. Inset (b): Conceptual section across the Northern Calcareous Alps, adapted from Kilian and Ortner (2019), and based on Bachmann and Müller (1981) for deep structure and well Vorderriss 1, and Freudenberger and Schwerd (1996).

the rheologic contrast between the décollement and the sedimentary succession above.

This study aims to answer the following questions using a mechanical numeric model:

- (1) Is it mechanically possible to buckle the sedimentary succession of the western NCA during shortening?
- (2) Does erosion and later re-sedimentation influence the development of buckle folds?

General analytical solutions for these questions have been presented by, e.g., Goff et al. (1996) and Schmalholz et al. (2002), however, our focus is to apply simple numerical modelling on the specific structural evolution of the western NCA.

1.1. Geologic setting

The NCA belong to the Eastern Alps and the term itself is a regional term, not implicating a tectonic unit. In a plate tectonic context, the NCA belong to the Alcapian plate (Handy et al., 2010), meaning a part of Adria, which includes continental and oceanic parts of a microplate between the European, Iberian and the African plate. From the Cretaceous on to the Early Cenozoic Alcapia was separated from Adria. Alcapia derives from Alcapa (Alps-Carpathians-Pannonian basin) including the Austroalpine units of the Eastern and Western Carpathians and remnants of the north-western margin of the Meliata-Maliac Ocean (Schmid et al., 2004). The NCA represent the most external units of the Austroalpine (e.g., Schmid et al., 2004; Tollmann, 1976b), and constitute a thin-skinned fold-and-thrust belt. The sedimentary succession of the study area spans the Permian to the Cretaceous.

1.2. Stratigraphic development (Fig. 2)

The Permian to Triassic sediments of the NCA were deposited on the passive continental margin of Pangea, facing the Meliata branch of the Neotethys ocean (e.g., Haas et al., 1995; Lein, 1987; Schmid et al., 2004; Stampfli et al., 1998). In the study area, the oldest sediments are Permian sediments (Haselgebirge) represented by grey shales, cellular dolomites and reddish to greenish quartz-rich sandstones which can be found in surface outcrops. In the subsurface, large amounts of anhydrite and gypsum are known and salt has been mined (Schmidegg, 1951; Spötl, 1989). Lower Triassic quartz sandstones (Alpiner Buntsandstein) which are intercalated by marls and clays (Tollmann, 1976a) follow the Permian succession. The Lower Triassic sandstones are in contact to the Anisian limestone and evaporites (Reichenhall Fm.), represented by cellular dolomites, stromatolitic dolomites and limestones. The cellular dolomites are the residue of sulphate evaporites in the subsurface.

Anisian to Ladinian limestones (Alpine Muschelkalk Group; Bechstadt and Mostler, 1976; Nittel, 2006; Rüffer and Zamperelli, 1997) follow above the last cellular dolomites. This massive to well-bedded succession of limestones interfingers in its uppermost part with the clinofolds of the Ladinian platform (Fig. 3a; Wetterstein limestone).

This Ladinian Wetterstein limestone is the first major carbonate platform in the NCA and reaches a thickness between 1700 m (Sarnthein, 1965) and 2200 m (Kilian and Ortner, 2019) in the Karwendel Mountains. Generally, the Triassic sedimentary succession has a layer-cake geometry on the kilometer-scale (except the clinofolds of the Ladinian platform), and this is spectacularly exposed in the almost 1 km high north-face of the Laliders cliffs (Fig. 3a; Kilian and Ortner, 2019). Thickness variations within the Alpine Muschelkalk Group and the Wetterstein limestone are probably a consequence of Triassic salt tectonics in the area. A succession of Carnian shales, limestone, dolomites and cellular dolomites (Northalpine Raibl Beds; Jerz, 1966) follows on top of the Wetterstein limestone.

In the Norian another major carbonate platform developed, the Norian Hauptdolomit, a well bedded, partly stromatolitic dolomite

(Fruth and Scherreiks, 1982; Müller-Jungbluth, 1971). Toward the top, this Norian platform drowns. Ultimately, drowning led to the formation of basins filled with marly limestone (Kössen Fm.) interfingering with platform carbonates (Oberrhät limestone; Golebiowski, 1991) during the Rhaetian.

The Jurassic sedimentation is controlled by rifting and the opening of the Alpine Tethys (Handy et al., 2010; Schmid et al., 2004). Alcapia, including the future NCA, was separated from Europe (e.g., Handy et al., 2010; Le Breton et al., 2021). The new continental margins drowned, ending shallow marine deposition, and pelagic sediments settled throughout the Jurassic and Early Cretaceous. Rift-related normal faulting caused major thickness differences in the syn-rift succession (Allgäu Fm.; e.g., Eberli, 1988; Jacobshagen, 1965; Nagel et al., 1976). Postrift deposition starts at the turn to the Upper Jurassic and includes variegated cherts (Ruhpolding Radiolarite; Diersche, 1980) and marly, well bedded, micritic limestones (Ammergau Fm.; Tollmann, 1976a). Lower Cretaceous to Oligocene sediments were deposited during Alpine shortening and are therefore synorogenic. Lower Cretaceous sediments (Berriasian to Albian) consist of marls occasionally intercalated with sandstones (Schrambach Fm.; Nagel et al., 1976).

The synorogenic Gosau Group of Late Cretaceous to Paleogene age, which is distributed over the whole width of the NCA unconformably overlies deformed older rocks (Faupl et al., 1987; Wagreich and Faupl, 1994) and documents Cretaceous erosion close to the present-day erosion surface. In the Karwendel mountains, the Gosau Group is not preserved. Clastic deposits in neptunian dykes occurring in the study area may be remnants of the Gosau Group (Krois and Stingl, 1994), or of Late Oligocene Molasse type foreland sediments (Inneralpine Molasse; Schmidegg, 1951). The sedimentary succession described here is the base for the numeric model and is determining the material characteristics of the layers of the model.

1.3. Deformation during alpine orogeny

Alpine orogeny is related to the closure of two oceans, the Neotethys and the Alpine Tethys (Handy et al., 2010):

- (1) Cretaceous orogeny occurred after obduction of Meliata ophiolites onto the southeastern Alcapian margin, with the Austroalpine, Alcapian-derived units being in lower plate position (Schmid et al., 2004; Stüwe and Schuster, 2010). The NCA had the position of a foreland fold-and-thrust belt.
- (2) Late Cretaceous shortening was related to subduction of the Alpine Tethys (Piemont-Liguria- and Valais ocean; Handy et al., 2010) with the Austroalpine units in an upper plate position. The NCA were carried piggy-back on top of a tectonically deeper detachment until collision occurred in the Late Eocene (Paleogene orogeny) (Schmid et al., 2004; Stüwe and Schuster, 2010). Within the internal Austroalpine basement units, Cretaceous and Paleogene orogeny is clearly separated by Upper Cretaceous extension (Froitzheim et al., 1994), but in the external thrust sheets (as the NCA are), Cretaceous to Cenozoic shortening is continuous, as documented by growth strata in different overlapping synorogenic successions (Ortner, 2001, 2003a, b; Ortner and Gaupp, 2007; Ortner et al., 2016).

The thrust sheets of the western NCA can be distinguished by their time of emplacement (Kilian and Ortner, 2019; Ortner, 2003a) using the youngest sediments below a thrust and transgression sediments on top of a thrust sheet. Nappe stacking in the western NCA started in the Lower Cretaceous, when the Karwendel thrust sheet moved onto the Tannheim thrust sheet between the Hauterivian and Albian on the Karwendel thrust (Fig. 1b). Thrusting propagated progressively into more external parts of the thrust belt, incorporating the Cenoman-Randschuppe in the Turonian, and the Rhenodanubian Flysch nappes in the Maastrichtian or Paleocene (Gaupp, 1982; Mattern and Wang, 2008; Ortner, 2003a).

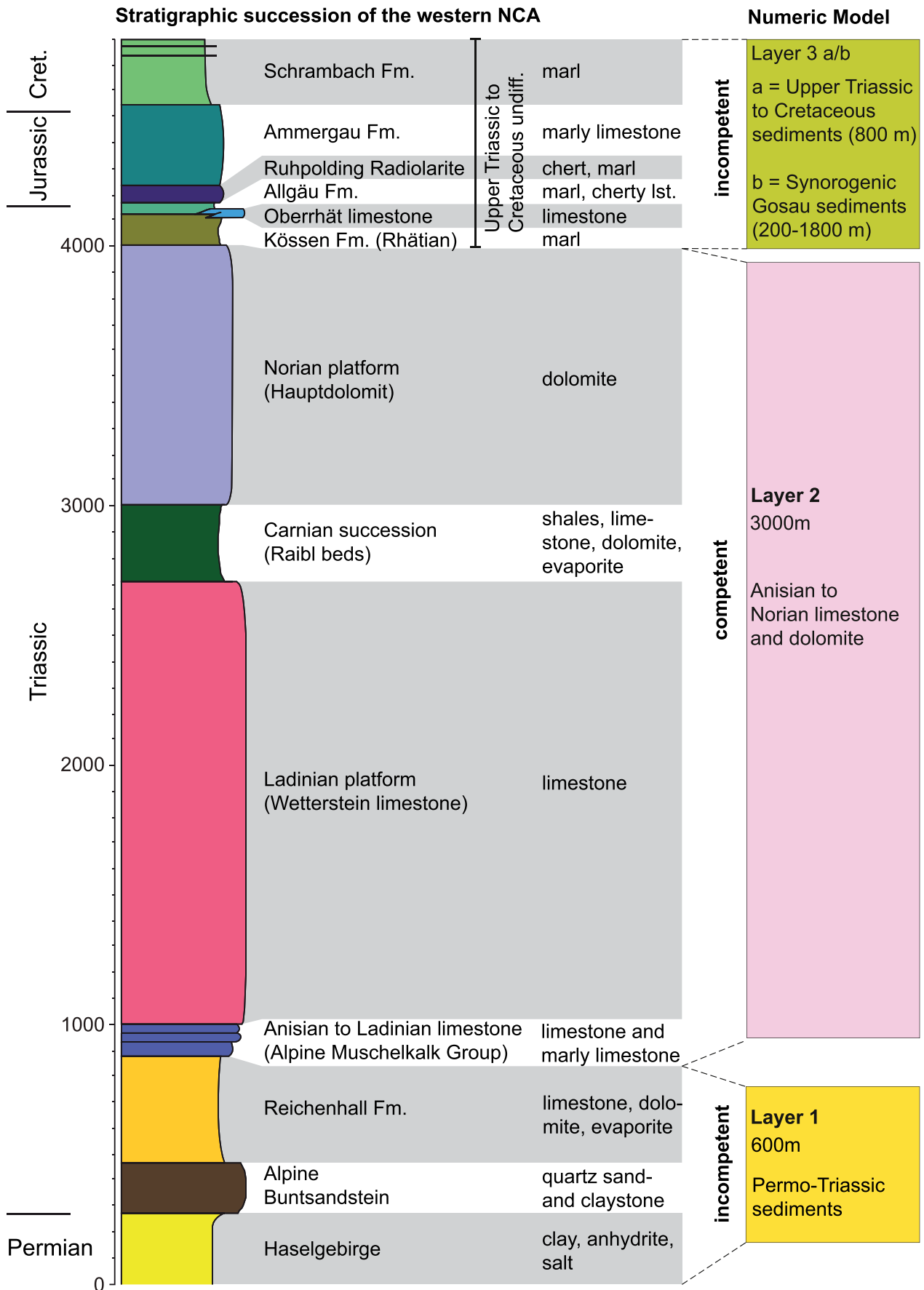


Fig. 2. Stratigraphic succession of the NCA in the study area and its translation to mechanically homogeneous layers of the numeric model. lst. = limestone.

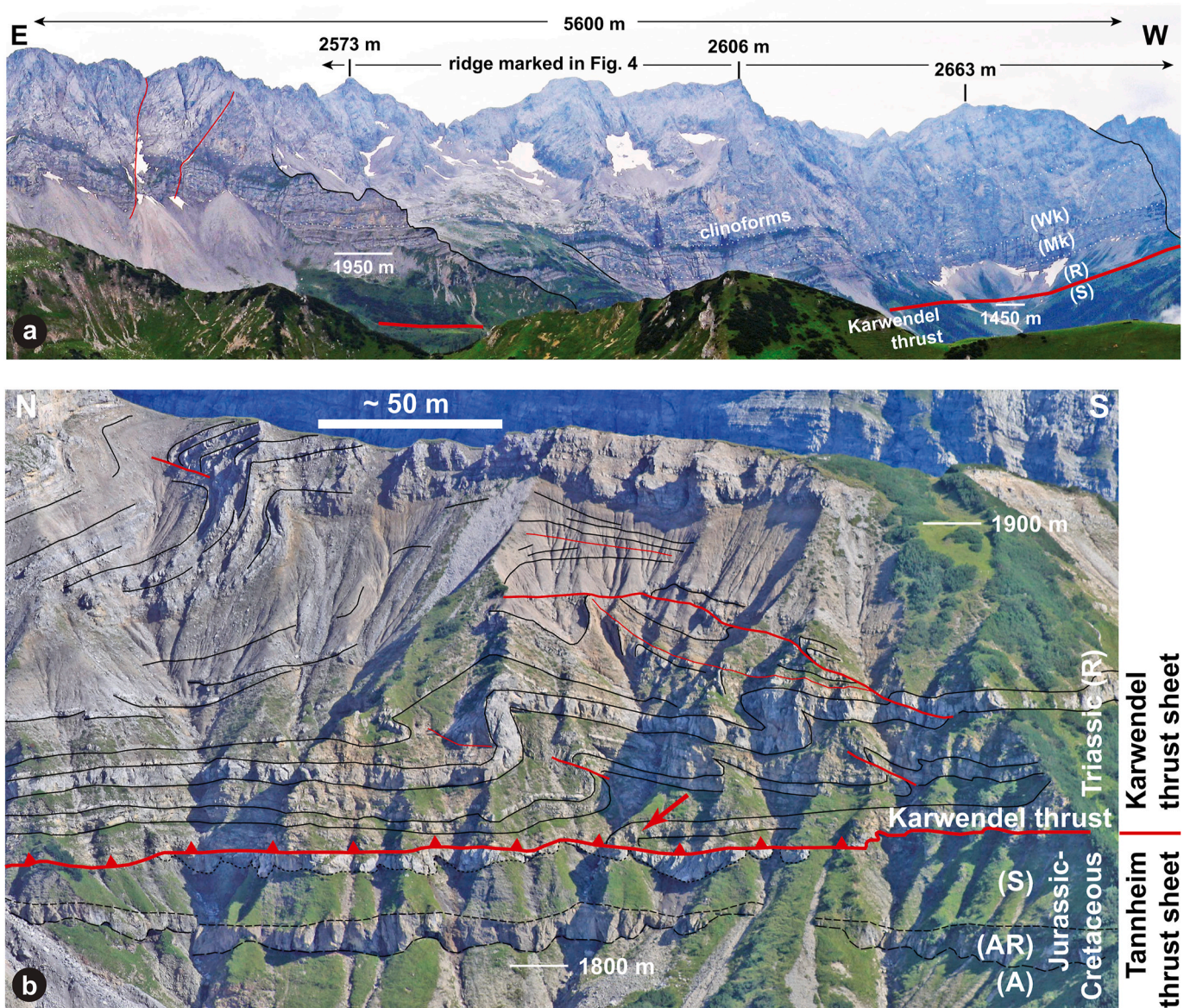


Fig. 3. Field photographs illustrating key aspects of local geology. **(a)** Panoramic view of the eastern 5 ½ km of the 900 m high Laiders cliffs from the north. The overcast weather prevents dark shadows in the north-facing cliffs. The cliffs provide a very oblique view of the Wetterstein clinoforms that interfinger with the uppermost part of the Alpine Muschelkalk Group to the southeast. Generally, the Triassic formations show a layer-cake stratal pattern. See Fig. 4 for location. **(b)** Key outcrop of the Karwendel thrust in the Karwendel mountains at Halftergraben, modified from Kilian and Ortner (2019) (see there for a detailed description). Abbreviations: R = Reichenhall Formation, Mk = Alpine Muschelkalk Group, Wk = Wetterstein limestone, A = Allgäu Formation, AR = Ammergau Formation and Ruhpolding Radiolarite, S = Schrambach Formation. Meter-scale buckle folds in Triassic sediments (Reichenhall Fm.) above the Karwendel thrust developed due to the competence contrast between carbonate beds and cellular dolomites. The Karwendel thrust is parallel to bedding in the immediate footwall and hanging wall, which is close to horizontal on hectometre scale. The thrust cuts the sedimentary succession of the hanging wall (Reichenhall Fm.) at a very low angle, truncating single beds (red arrow). See Figs. 4 and 5a for location. (For interpretation of the references to colour in this figure legend, the reader is referred to the Web version of this article.)

Early Cretaceous nappe stacking and transport was NW- to NNW-directed, while subsequent Late Cretaceous to Paleogene shortening was N- to NNE-directed (Eisbacher and Brandner, 1996; Ortner, 2003a). Late Paleogene to Neogene shortening was NE-directed (Ortner, 2003b; Peresson and Decker, 1997).

After Early Cretaceous thrust sheet emplacement, the thrusts of the NCA started to be folded as the active detachment shifted into the footwall. This process is related to antiformal stacking in the tectonically deeper units (Fig. 1b). Locally, thrusts breaking across these folds evolved. Shortening can be as young as Miocene (Kilian and Ortner, 2019).

As a consequence of nappe stacking in the NCA and thickening of the

orogenic wedge, regional erosion prior to deposition of synorogenic sediments affected the NCA (Gaupp, 1982; Ortner and Gaupp, 2007; Wagreich and Faupl, 1994). The Cenomanian to Campanian Branderfleck Fm. and the Turonian to Eocene Gosau Group of the western NCA are found in growth synclines that document the folding process (Ortner, 2001; Ortner and Gaupp, 2007; Ortner et al., 2016), during which also the thrusts were folded. Folding of Molasse sediments related to the wedge-top of the Alpine foreland basin of Late Eocene to Oligocene age points to ongoing shortening into the Miocene (Ortner et al., 2006; Ortner and Stingl, 2001).

1.4. Local tectonic setting

We studied the Karwendel thrust and the overlying Karwendel thrust sheet in the Karwendel Mountains (Fig. 1) of the western NCA. The Karwendel thrust was one of the first thrusts of the NCA recognized at the beginning of the 20th century (Ampferer, 1902). It emplaces Permian to Triassic rocks on top of Cretaceous rocks (Fig. 3b). The thrust follows the Permian evaporites (remnants of salt bearing Haselgebirge), but is mostly found at the base of the Triassic succession of the hanging wall (Reichenhall Fm.; Fig. 3b). Only in the southernmost part of Karwendel Mountains larger volumes of the Permian succession (Haselgebirge) are preserved (Figs. 1 and 4).

In the Karwendel Mountains, Cretaceous nappe stacking was NW-directed. Mesoscale observations showed that shortening directions changed from NW (Lower Cretaceous) to N to NE in the Paleogene (Kilian and Ortner, 2019). The Karwendel thrust is parallel to bedding in the immediate footwall and hanging wall on local (Fig. 3b; Kilian and Ortner, 2019) and regional scale (Fig. 1b). However, the hanging wall succession above the thrust is folded on the kilometer-scale (folds labelled (1) in Figs. 4 and 5). The W- to WNW-trending fold axes of these

km-scale folds suggest a Paleogene age (e.g., Eisbacher and Brandner, 1996). Folds above the thrust plane are therefore younger than the Karwendel thrust, which is of Cretaceous age. This suggests that at least parts of the hanging wall were decoupled from the footwall during ongoing deformation after the emplacement of thrust sheets (Kilian and Ortner, 2019). The shape of the folds with round hinges and the accumulation of weaker material in the core of the folds (Fig. 5b) suggest that the folds are buckle folds caused by rheological differences between the décollement (Permo-Triassic evaporites) and the competent sedimentary succession above (Anisian to Norian carbonates). Some of the folds in the area re-fold the Karwendel thrust (folds labelled (2) in Figs. 4 and 5). These folds need another, tectonically deeper décollement and might be related to Late Cretaceous or Paleogene duplexing below the Karwendel thrust sheet (Fig. 1b).

The Karwendel thrust sheet was affected by erosion down to the Ladinian platform prior to transgression of the Cretaceous (Krois and Stingl, 1994; Ortner, 2003a). Alternatively, these deposits are part of a Paleogene sedimentary cover (Inneralpine Molasse; Frisch et al., 2001; Schmidegg, 1951). Therefore, folding took place after a decrease in overburden in the late Early Cretaceous. Late Cretaceous syntectonic

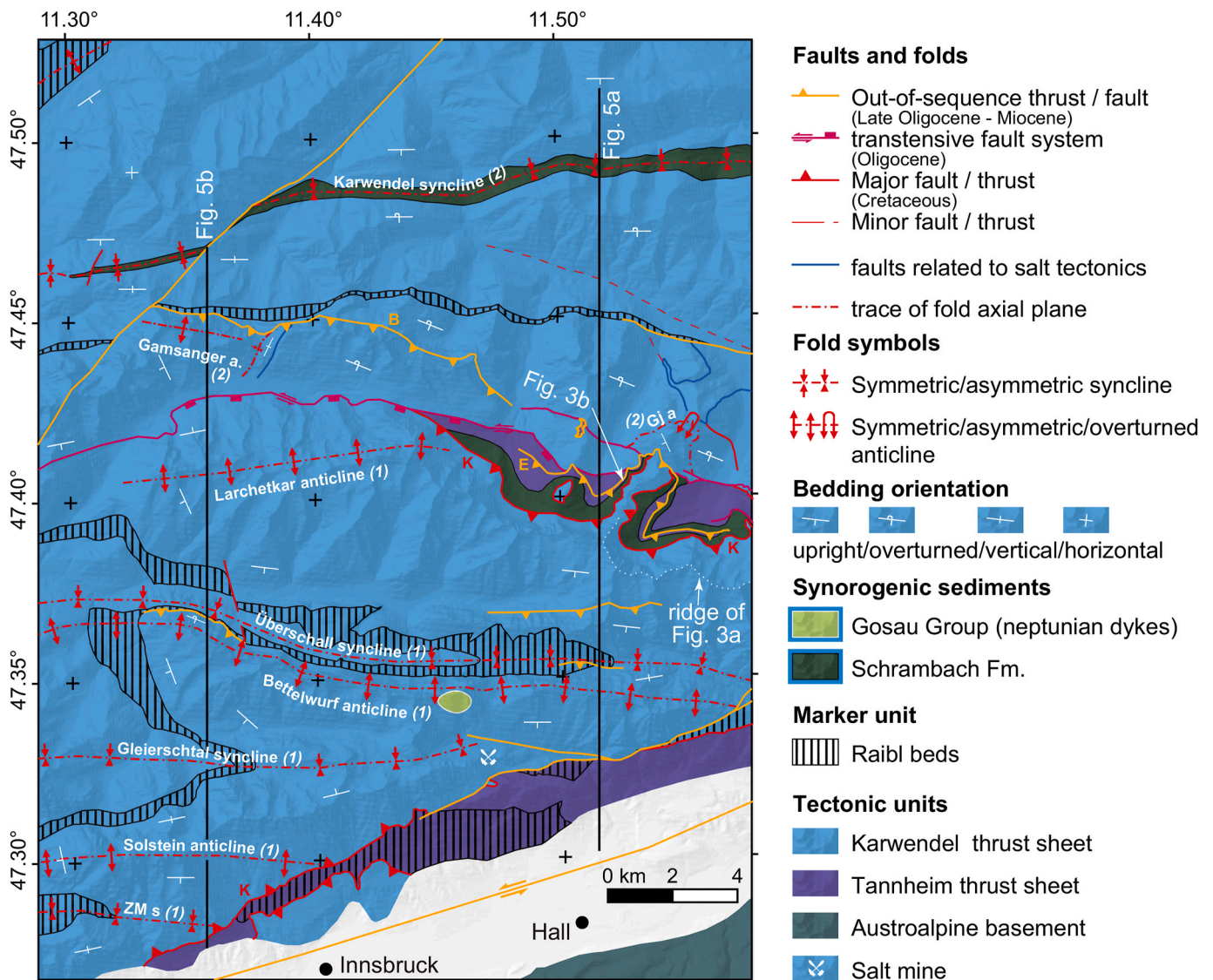


Fig. 4. Tectonic map of the Karwendel mountains north of Innsbruck. See Fig. 1 for location. The Raibl marker is emphasized by the vertical hatch and illustrates the km-scale folds. Faults are grouped into several successive generations based on the structural analysis of Kilian and Ortner (2019). Fold names according to Tollmann (1976b). Abbreviations: B = Bäralpl thrust, E = Eng thrust, K = Karwendel thrust, Gj a = Gamsjoch anticline, ZM s = Zirler Mähder syncline, a. = anticline.

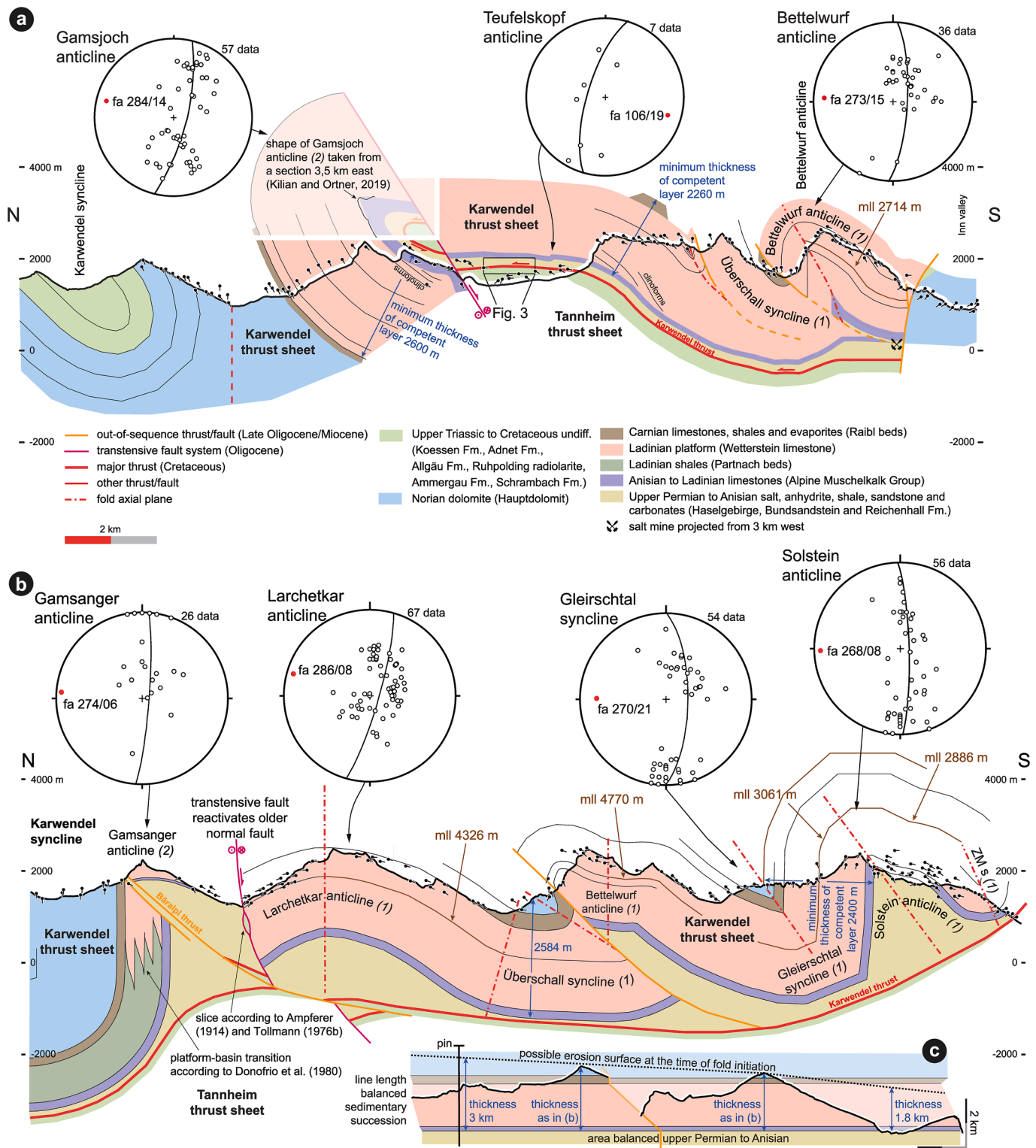


Fig. 5. Two N–S cross sections of the Karwendel mountains. See Fig. 4 for location. Open to tight folds are restricted to the hanging wall of the Karwendel thrust. All folds are interpreted to have formed during Paleogene N–NNE shortening. The thrust is gently folded and locally offset by transpressive normal faults. Abbreviations: fa = fold axis, mll = measured limb length, ZM s = Zirler-Mähder syncline. (a) Cross section 1. Tight folds are only found close to the southern end of the section. The very tight appearance of the Gamsjoch anticline results from the projection of a section 3.5 km to the east into this section, where the anticline has an opening angle of 90°. The projected fold demonstrates the continuity of structures prior to the normal offset. (b) Cross section 2 depicts a fold train of four anticlines and intervening synclines. The upper Permian to Anisian units of the décollement fill the anticline cores. These folds are the main target of this study. Interfingering of Ladinian platform and basin according to the observations of Donofrio et al. (1980), slice of Upper Triassic to Cretaceous associated with transpressive fault following Ampferer (1914) and Tollmann (1976b). (c) Balanced version of (b) south of the transpressive fault. The axial plane of the Larchetkar anticline was used as a local pin.

sediments (Gosau Group) record Late Cretaceous–Paleogene folding (Auer and Eisbacher, 2003; Ortner, 2001, 2003a; Ortner and Gaupp, 2007; Ortner et al., 2016).

1.5. Buckle folding

Buckle folds develop due to rheological differences in layered rock and scale from millimetres to kilometres (e.g., Abbassi and Mancktelow, 1992; Biot, 1961; Ramsay and Huber, 1987; Sherwin and Chapple, 1968). Buckle folds of isolated competent layers in a weaker matrix are quite common (e.g., Hudleston and Holst, 1984; Schmalholz and Mancktelow, 2016; Sherwin and Chapple, 1968). Large-scale, i.e., meters to few kilometres-size buckle folds are usually referred to as detachment folds (Jamison, 1987), which develop due to shortening and/or shearing of multilayers above a basal décollement (Butler et al., 2020; Rowan and Kligfield, 1992).

The end-member of the buckle fold theory for multilayers with a low proportion of incompetent to competent layer thickness and a high viscosity contrast between competent and incompetent layers is comparable to the geometry of fault-bend folding (Johnson and Fletcher, 1994; Ramsay and Huber, 1987; Schmalholz and Mancktelow, 2016 and references therein). In regional studies on the geometry and kinematics of fold-and-thrust belts, a continuous transition from thrusting with fault-bend folding to buckle folding on top of a décollement has been observed (e.g., Ortner et al., 2015; Pfiffner, 1993).

There exists a wide range of numerical simulations on buckle folds (e.g., Fehner, 2011; Lan and Hudleston, 1991; Llorens et al., 2013; Schmalholz and Schmid, 2012). Most models describe the fold shape analytically in different settings (single layer, or multilayer) with different material rheologies (elastic, visco-elastic, viscous) (e.g., Biot, 1961; Biot and Taylor, 1957; Ghassemi et al., 2010; Huang et al., 2010; Ramberg, 1963; Schmalholz and Schmid, 2012). Already Biot (1961) found that the wavelength (or arc length) of buckle folds depends on the competence contrast of the buckling layer (competent layer) and the surrounding matrix (incompetent layer). Generally, small-scale folds can ignore the effect of gravity whereas the development of large-scale folds is gravity dependent. In nature, both matrix and gravity resist folding. Schmalholz et al. (2002) plotted the ratio between competent layer and surrounding matrix thickness against the ratio between fold wavelength to total thickness and was able to distinguish between gravity-controlled, matrix-controlled and detachment folding.

2. Numerical modelling

Our numerical modelling did not aim to reproduce nature. Instead we tried to test a few parameters that we regarded to be important, using a series of models in which these parameters were varied. These parameters are: Thickness of a competent layer above a weak décollement, thickness of a weak overburden, rheology of the different layer and here especially ratios of stiffness for competent/incompetent rock.

2.1. Model set up: from field to model

The numeric model is based on the sedimentary record of the hanging wall and the material characteristics of the layers. Generalizing the sedimentary succession, we distinguish three rheologically different layers. Describing the rheology of the layers, we differentiate between incompetent and competent rock (Fig. 2).

2.1.1. Layer 1

The décollement of the Karwendel thrust sheet are Permian to Triassic sediments (Haselgebirge, Alpiner Buntsandstein, Reichenhall Fm) and therefore the original thickness is not preserved. In the Halltal area (indicated by the salt mine in Figs. 1 and 5a) the strongly deformed Permian succession is exposed at the Karwendel thrust. Cross sections of the Halltal area show a present-day thicknesses of at least 200–700 m

(Schmidegg, 1951), but the original stratigraphic thickness is difficult to assess due to tectonic deformation (Leitner and Spötl, 2017; Schaubberger, 1986; Tollmann, 1976a). Salt itself flows over geologic time scales (Jackson and Hudec, 2017), causing thickness and distribution variations of salt bodies and within the overlying Triassic sediments (e.g., Granado et al., 2018).

In the southern part of the Karwendel Mountains, remnants of the Lower Triassic rocks (Alpiner Buntsandstein) are found at the décollement. In the most parts of the western NCA, however, Triassic cellular dolomites and dolomites of the Reichenhall Fm (Miller, 1965; Nagel et al., 1976). are the basal unit on top of the décollement (see Fig. 3b). In the study area the Permo-Triassic succession is truncated at the base by the Karwendel thrust (marked with a red arrow in Fig. 3b). The remaining thickness on top of the thrust is 300 m. However, it may have been significantly thicker prior to thrust transport. Area-balancing the Permo-Triassic evaporitic succession on top of the Karwendel thrust of Fig. 5b allows to calculate a thickness of 580 m between Bettelwurf anticline and Zirler-Mähder syncline prior to folding, and 530 m below Larchetkar anticline and Überschall syncline (Fig. 5c). These values are minimum values dependent on cross section construction. During modelling, we tested the influence of boundary effects. In pilot models 600 m of thickness sufficed to minimise boundary effects from the bottom line, when using a mesh width of 200 m (see chapter 2.4, and Fig. 6). Therefore, we ultimately decided to use 600 m of thickness for the incompetent layer 1 as the real thickness remains unknown.

2.1.2. Layer 2

The Anisian to Ladinian limestone, the Ladinian carbonate platform, the Carnian shales and the Norian dolomites, follow above the Permo-Triassic succession. The Anisian to Ladinian limestone (Alpine Muschelkalk Group) is up to 500 m thick (Frisch, 1975; Miller, 1965). The thickness of the Ladinian carbonate platform (Wetterstein limestone) is variable, as the platform interfingers with basinal sediments in variable directions (e.g., Sarnthein, 1967). Up to 2200 m are present in the study area (Kilian and Ortner, 2019). Sarnthein (1965) measured a thickness of 1730 m for the Ladinian carbonate platform in the Karwendel Mountains north of Innsbruck. Based on 3D-modelling, Ortner (2015) deduced a thickness of 1400 m (measured) for the Ladinian carbonate platform in the Zugspitze massif of the Wetterstein Mountains (Fig. 1), however the contact to the Carnian succession at the top is eroded. An average thickness of 1500 m represents the Ladinian carbonate platform in the model.

The Carnian succession, with approximately 400 m, appears between the Ladinian carbonate platform and the Norian dolomite. We omitted the Carnian rocks as an incompetent layer in the model because we assumed that the thick competent units (limestone and dolomite) determine the rheology. We did this for following reasons: Measured stratigraphic sections in the area (e.g., Brandner and Poleschinski, 1986; Jerz, 1966) show that a large part of the Carnian succession consists of limestones and dolomites (more than 55%), and shales and cellular dolomites comprise less than 20% and 25%, respectively. The succession is not observed to act as a décollement anywhere in this internal part of the NCA. This is in contrast to the externmost NCA where the Ladinian platform is replaced by shales and these combined Ladinian-Carnian shales are one of the principal décollements (Fig. 1b) (Auer and Eisbacher, 2003; Eisbacher et al., 1990; Linzer et al., 1995). We performed sensitivity tests during modelling to understand the influence of such a layer. To test the possible influence of an incompetent unit intercalated in the thick competent layer 2, we performed model runs with a model setup similar to the models of Fig. 7a. We inserted an incompetent layer in the lower third of the competent unit having the same material parameters as the basal incompetent unit. Upon shortening, two anticlines developed, having limb lengths even larger than the limb lengths in model of Fig. 7a.

For the Norian dolomite (Hauptdolomit) Miller (1963) described 1000 m of thickness in the Mieming Mountain chain. Donofrio et al.

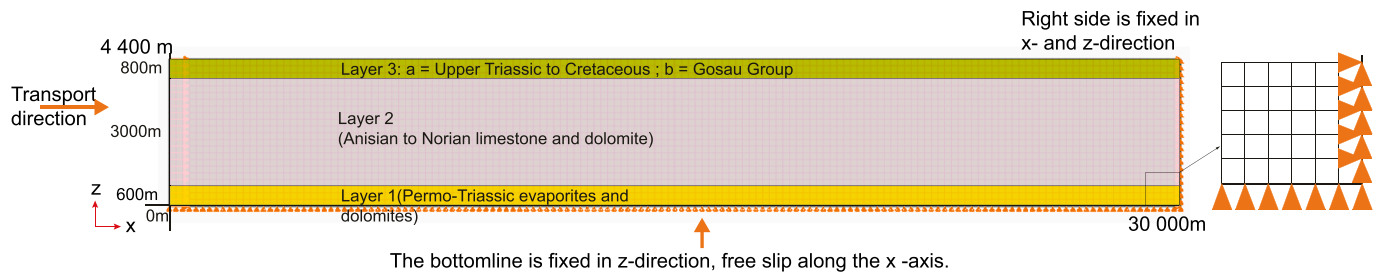


Fig. 6. Undeformed three-layer model. The element size is 200×200 m, all elements together build the mesh. All length units in the model are given in meters. Orange triangles show the boundary conditions, the tip of the triangle indicates the fixed direction (see magnified detail to the right). The bottom line is fixed in z-direction, the right side is fixed in x- and z-direction. (For interpretation of the references to colour in this figure legend, the reader is referred to the Web version of this article.)

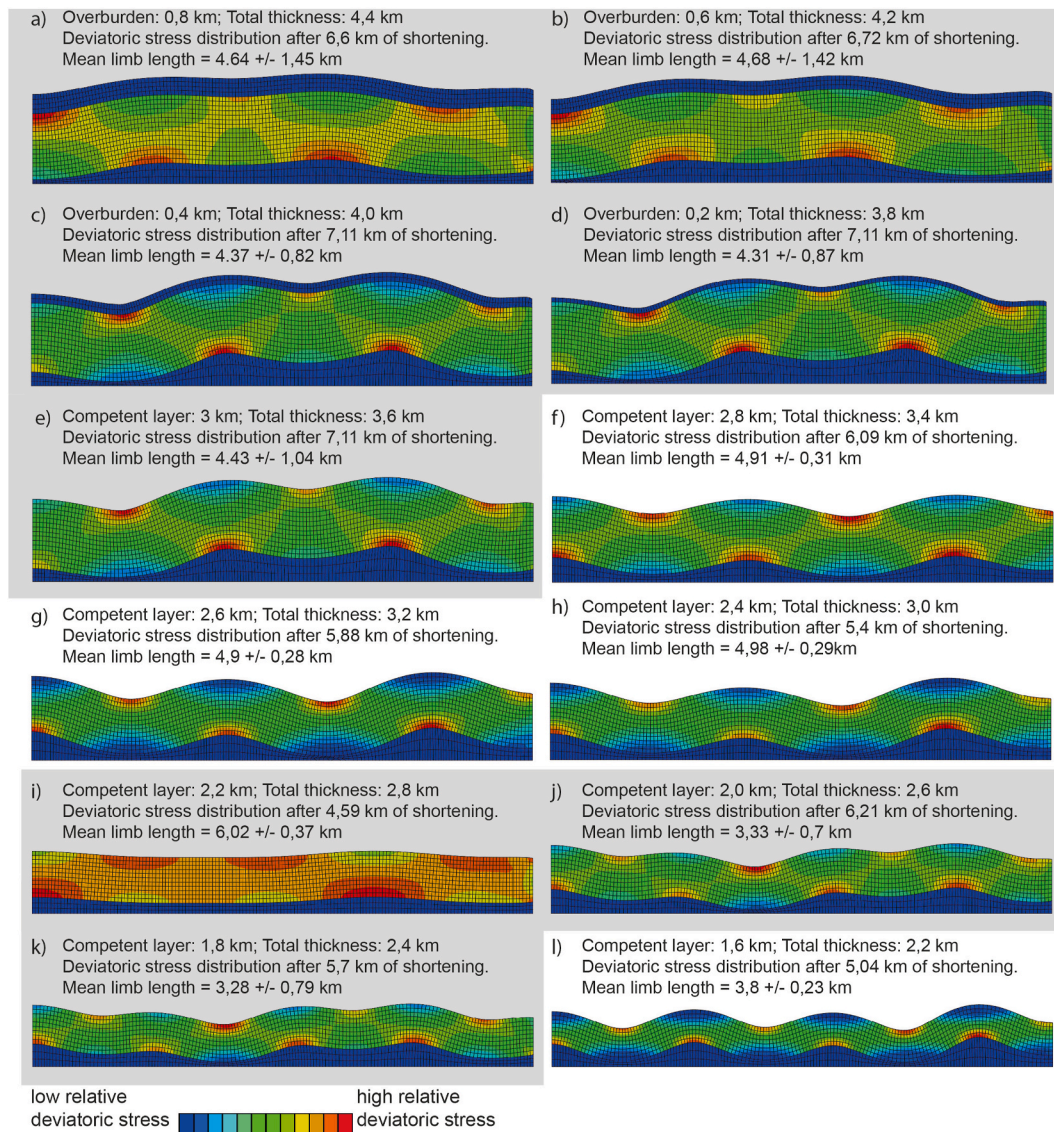


Fig. 7. Results of erosion modelling. The material model is linear elasticity. Coloration represents the relative deviatoric stress distribution. Erosion removes progressively more element rows starting at the top in (a). Material parameters: Layer 1 (bottom): E-Module 2 000 000 kN/m², Poisson ratio 0.25; Layer 2 (middle): E-Module 80 000 000 kN/m², Poisson ratio 0.2; Layer 3 (top): E-Module 10 000 000 kN/m²; Poisson ratio 0.25. The grey background indicates models with irregular fold geometries (for explanation see chapter 3.3.1).

(2003) observed 2700 m in the Karwendel Mountains close to Seefeld (Tirol). Behrmann and Tanner (2006) specified 700–2500 m. The thickness of the Norian dolomite varies in the NCA, for the model we

used a thickness of 1000 m defined by Miller (1963) for the Mieming Mountains because in the Karwendel the upper part of the Norian dolomite mostly eroded and the real thickness is speculative. In total the

competent layer 2 has a thickness of 3000 m.

2.1.3. Layer 3

Layer 3 represents the sedimentary cover on top of the competent layer 2. The Upper Triassic to Lower Cretaceous succession, which is preserved in the northern part of cross section 1 (Karwendel syncline of Figs. 4 and 5a) is represented by layer 3a. Because erosion exhumed the Ladinian platform carbonates to the surface during nappe stacking and the Gosau Group (layer 3 b) was sedimented on top of layer 2 we modelled two scenarios:

In scenario (1) the sedimentary succession of the upper thrust sheet continues with shallow marine to pelagic sediments of the Upper Triassic to the Cretaceous (Kössen Fm, Oberrhät limestone, Allgäu Fm, Ruhpolding radiolarite, Ammergau Fm. and Schrambach Fm; Fig. 2). This is represented by the Layer 3a, which assumes continuous sedimentation throughout the Late Triassic into the Early Cretaceous. Layer 3a is incompetent, as the only competent unit, the Oberrhät limestone is thin, and it is absent in much of the area (Nagel et al., 1976; Palotai et al., 2017). We used a thickness of 800 m for layer 3a based on Palotai et al. (2017) and Nagel et al. (1976).

In scenario (2) we modelled the synorogenic Gosau Group, which was deposited unconformably on top of the NCA orogenic wedge after initial nappe stacking and related major erosion (e.g., Ortner, 2003a; Wagreich and Faupl, 1994). The Gosau group is represented by layer 3 b in the model. For modelling scenario 2 we removed layer 3a, and parts of layer 2. The Gosau Group Material characteristics of layer 3 b are comparable to layer 3a. The thickness is highly variable, and dependence on faulting (Wagreich and Decker, 2001) or folding has locally been demonstrated (Ortner, 2001; Ortner et al., 2016). In spite of the present-day patchy distribution (Fig. 1), the Gosau Group is regarded to represent erosional remnants of an originally continuous sedimentary cover (Wagreich and Faupl, 1994).

Even though no synorogenic Gosau sediments were observed in the immediate study area, we modelled them because in the Karwendel Mountains neptunian dykes of potential Late Cretaceous age were observed (Fig. 1a; Krois and Stingl, 1994). Alternatively, these dykes are of Paleogene age (Schmidegg, 1951). For the model, we used different thicknesses for layer 3 b from 200 m to 1800 m, based on the thickness of the sedimentary successions of the Gosau Group at Brandenberg to the east (Sanders, 1998; Sanders and Höfling, 2000) and Mutteköpf to the west (Ortner, 2001; Ortner et al., 2016).

2.2. Model realisation

The numeric simulations were realised with the finite element software Abaqus. Abaqus is a program designed for problems of solid mechanics and dynamics using a continuum approach. It allows interactive designing of models, running the models and analysing the results. Abaqus works dimensionless meaning the user has to define a coherent unit system, which is important when defining material parameters. Finite element methods (FE-Methods) are numeric solutions for problems with infinite degrees of freedom. By discretisation, the degrees of freedom become finite. A determined number of elements represents the complex model. Abaqus has been used previously successfully in studies on rock deformation (e.g., Eckert et al., 2014; Guest et al., 2007; Huang et al., 2010; Jeng et al., 2002; Liu et al., 2016).

The rheology of rocks is described as an elastic material model. The material model describes the deformation behaviour of the material in dependence of the acting stresses. The rheology is thereby defined by material parameters. The material parameters for linear elastic models are expressed by the Young's modulus (E-module) and the Poisson ratio. In geologic literature, the materials are often generalised as competent and less competent or incompetent rocks (e.g., Ramsay and Huber, 1987). In the numeric model the competence is expressed by a higher E-module (stiffer) and smaller Poisson ratio for competent rocks and a lower E-module (less stiff) and a slightly higher Poisson ratio for

incompetent rocks. However, no sensitivity analyses on the effect of the Poisson's ratio was performed in this study. As in this study the focus was on fold nucleation, the driving factors were differences (ratios) in stiffness between the single layers in combination with the thickness of those layers. A quantitative evaluation of stresses is therefore not possible. The linear elastic material model was used for the following reasons:

- (1) The focus was on modelling folding (deformation) and not on faulting (failure). A material model that includes a failure criterion could be used for modelling faulting but stops the calculation before folding can develop. The folding influences the limb length formation and is a result of ratios of stiffness and thickness of the single layers. Do to the used elastic model, it is not possible to evaluate the stresses, especially those close to the surface as those stresses are strongly influenced by local failure mechanism.
- (2) During nucleation of buckle folds in the early stage of shortening, when limb length is determined, most probably elastic deformation prevails (Jeng et al., 2002; Price and Cosgrove, 1990). Viscous deformation plays an important role in the later stages of deformation.
- (3) Structural data showed that the large km-scale folds of the Karwendel Mountains formed during Paleogene shortening, and not during Lower Cretaceous stacking of nappes (compare Kilian and Ortner, 2019). As a consequence of erosion following nappe stacking, we suggest a free surface at the time of the development of folds. At shallow levels, rocks deform elastically (Jeng and Huang, 2008).
- (4) The numeric model focused on the development of folds in dependence of rheological contrasts. Time was not considered, as is done in the case of viscous rheology. For the simulations a virtual time was modelled. Therefore, no statement on time scales can be derived from the model. Providing this virtual calculation time, ratios of viscosities of a linear viscous model coincide with the ratios of stiffnesses (Young's moduli) of a linear elastic model. As outlined above the studied folds are buckle folds, contemporaneous flexural slip is possible but neglected in the model.

The model is a 2D plane strain model. Plane strain assumes no change in geometry with depth. This holds for problems where the variation with depth is not meaningful. Simplicity and a quick change of possible settings stood in the foreground.

2.3. Material parameters

The model consists of three layers whereas each layer has different material characteristics but is in itself homogeneous. The Young's modulus and the Poisson ratio determine the rock parameters in elastic material models. The Young's modulus (E-module) is given in kilo Pascals (kPa), the Poisson ratio is dimensionless. Rock parameters derive from geotechnical tests of homogenous rock samples and are always just an approximation of natural properties of rocks.

In contrast to previous models (e.g., Huang et al., 2010; Jeng et al., 2002; Llorens et al., 2013; Mancktelow, 1999), we abstained from pre-defining perturbations in the model to produce folds as has been done in other studies (e.g., Jeng et al., 2002; Schmalholz and Schmid, 2012).

Homogeneous layers, as used in the model, do not reflect a natural rock state, single perturbations neither. Scattering rock parameters within the layer would be a possibility to come closer to a natural state of rocks (e.g., Moulas and Schmalholz, 2020). In such a case, each layer has a defined range of values, and then each element of the layer gets a random value out of the defined range.

In pilot models, we tested the influence of the defined layer parameters (Young's modulus and Poisson ratio for linear elastic models) on the possibility of folding. According to these pilot tests, competence contrast and the material parameters of the basal layer 1 control the

ability of folding. Material parameters were chosen according to pilot models and published data (e.g., Czech and Huber, 1990; von Soos and Engel, 2008; see Table 1). However, not the values itself are relevant for this study, rather the ratios in stiffnesses and the ratios of layer thicknesses are relevant for folding. In addition, measurements of strength and stiffness in the laboratory are only possible on rock samples. These values do not apply for rock masses as they are observed in field.

The basal layer 1 represents the Permo-Triassic evaporites (Haselgebirge, Alpiner Buntsandstein, Reichenhall Fm.). Published material parameters for the Young's modulus have values ranging from 4.500.000 to 28.600.000 kN/m² for the Permian evaporites (Haselgebirge; Czech and Huber, 1990). Li (2013) modelled the E-module for salt in triaxial numeric experiments and calculated a value of 10 GPa (1.000.000 kPa, at temperatures of about 50 °C).

Our chosen value is 2.000.000 kPa because we do not know how much salt was in the system and we assume a mixture of salt and marls is the detachment horizon (see chapter 1.2). This value turned out to work best in the pilot models. If the E-Module is too high, the competence contrast between layer 1 and 2 is too low for buckling. If the E-Module is too low, only the base layer deforms until the large gradient in stresses between the layers stop calculation before layer 2 is folded.

2.4. Discretisation

Discretisation is the process that divides the whole model in sub-domains, in this case in elements. All elements are plane strain elements with four nodes. Plane strain elements simulate strain in x- and z-direction, therefore only vertical and horizontal strain can be applied. Elements connect through nodes to build a mesh (Fig. 6). The size of each element is 200 × 200 m. In pilot models, the influence of element size was tested: bigger elements reduced calculation time but also the accuracy of the results, small elements increased the calculation time but also the resolution of deformation. The used size is a compromise between calculation time and resolution. Fold limb lengths were not influenced by the larger mesh.

2.5. Boundary conditions

The boundary conditions define the freedom to move for the elements in the model. All elements can move in x- and z-direction, except fixed nodes of the elements. As the elements are four node-elements, any node can be fixed in x- and/or z-direction. The decision about the fixed nodes bases on an assumed behaviour of a thrust sheet. Along the bottom line, the model is fixed in vertical (z) direction but free to move in horizontal (x) direction. There is no friction across the bottom line, supposing that the thrust sheet slides along the décollement horizon. The model top surface is free, as folding happens after the emplacement of the hanging wall thrust sheet. The right side of the model is fixed in x- and z-direction, because structural studies in the Karwendel Mountains showed that buckling of the hanging wall stops when the hanging wall and footwall are folded together (Kilian and Ortner, 2019). The model is thrust in x-direction from the left side.

Table 1

Selected values from literature review and values used for the simulation. The used values are composed values from published data and pilot-tests.

Values from literature			Values used for the model			
Rock	E-module (kPa) Czech and Huber (1990)	Poisson ratio (von Soos and Engel, 2008)	Layer	Layer thickness (m)	E-module (kPa)	Poisson ratio
Lower upper Cretaceous rocks (Schrambach Fm.)	31 000 000	clay shales: 0.3	Layer 3 (TOP)	800	10 000 000	0.25
Norian dolomite (Hauptdolomit)	37 000 000 - 51 100 000	dense limestone: 0.2	Layer 2 (MIDDLE)	3000	80 000 000	0.2
Permian evaporites (Haselgebirge)	4 500 000 - 28 600 000		Layer 1 (BOTTOM)	600	2 000 000	0.25

2.6. Initial stress distribution

Before the model is shortened in x-direction, it is important to define the initial stress distribution to reach an equilibrium at the beginning. We applied the geostatic stress caused by gravity, which is divided into a vertical (z) and a horizontal (x) component. The initial stress distribution depends on the height of the model and the material parameters of the layers. The model starts with an initial stress state free of deformation.

2.6.1. Calculation of the vertical stress at rest

The vertical stress is equal to geostatic stress or lithostatic pressure and defined by the model height (z) and the specific weight of the rock volume (γ).

$$\text{Specific weight: } \gamma = \rho^* g$$

$$\text{Density: } \rho = 2850 \frac{\text{kg}}{\text{m}^3}$$

$$\text{Gravity: } g = 10 \frac{\text{m}}{\text{s}^2}$$

$$\gamma = 2850 \frac{\text{kg}}{\text{m}^3} * 10 \frac{\text{m}}{\text{s}^2} = 28500 \frac{\text{kg} \cdot \text{m}}{\text{m}^3 \cdot \text{s}^2} = 28500 \text{ N/m}^3; \gamma = 28,5 \text{ kN/m}^3$$

Eq. (1)

There is no vertical stress at the top because the surface is free ($\sigma_{top} = 0$). The vertical stress (or geostatic stress) increases with the depth and is here exemplarily calculated for a model with 4000 m height:

σ_{bottom} = model height (z) * ($-\gamma$); (The algebraic sign is minus because the force acts in the negative z-direction ↓)

$$\sigma_{bottom} = 4000 \text{ m} * (-28.5 \text{ kN/m}^3) = -114\,000 \text{ kPa} \quad \text{Eq. (2)}$$

2.6.2. Calculation of the horizontal stress at rest

The horizontal stress is dependent on the vertical stress and the coefficient of the earth pressure at rest (K_0). The defined horizontal stress reflects the stress of the material caused by lithostatic pressure.

Horizontal stress:	$\sigma_h = K_0 * \sigma_z$
	$\sigma_z = \sigma_{top} + \sigma_{bottom}$
	$\sigma_{z\ top} = 0$
	$\sigma_{z\ bottom} = z^* \gamma$

Coefficient of earth pressure at rest (K_0):

$$K_0 = \frac{\vartheta}{(1 - \vartheta)}$$

The Poisson ratio ϑ derives from the geotechnical tests and is for the incompetent material 0.3, for competent material 0.2 (von Soos and Engel, 2008). We calculated the horizontal stress here exemplarily with a

mean value of $\vartheta = 0.25$.

Poisson ratio:	$\vartheta = 0.25$
	$K_0 = 0.33$

The horizontal stress is calculated in each row of cells in the mesh using the model height of the row. It is calculated here exemplarily for a depth of 2000 m in a model 4000 m high. For other model thicknesses, due to erosion or resedimentation, the stress has to be recalculated accordingly.

$$\sigma_h = K_0 * \sigma_z$$

$$\sigma_h = 0.33 * \left(\frac{4000}{2} * 28.5 \right) = 18\,810 \text{ kN/m}^2 \quad \text{Eq. (3)}$$

2.7. Thrust amount

The model was pushed in horizontal direction from the left side. The minimum thrust distance in the Karwendel Mountains is about 38 km (Kilian and Ortner, 2019), excluding folding and late out-of-sequence thrusting. Because folding postdated the emplacement of thrust sheets, and the focus of modelling was folding and not thrusting, we shortened the model without a specific limit. However, the reached shortenings for the different models were in a close range mostly due to the automatic incrementation (applied shortening for each calculation sub step), a maximum shortening of approx. 7 km was reached in the models (Figs. 7

and 8).

2.8. Erosion and sedimentation

As described above, erosion and later sedimentation (Gosau or Inneralpine Molasse sediments) was contemporaneous with folding. We considered erosion and sedimentation in the numeric model using model series in which each model had different thicknesses of the competent layer and different thicknesses of overburden. Each individual model was set-up before deformation, and no erosion or resedimentation was applied progressively during shortening.

The model series started with the maximum thickness of all three layers. Successive erosion was modelled by removing element rows from layer 3a and layer 2 until the latter was almost half as thick (1600 m) as compared to its initial thickness (3000 m). Removing one row of elements led to 200 m of erosion. The re-sedimentation starts on top of the eroded competent unit. New element rows (layer 3 b) were added in each calculation on top of the eroded units. Given by the element size it starts with 200 m and reaches up to 1800 m syntectonic sediments. For each geometrical setting a new model with own initial stress state was used.

3. Results

Modelling erosion and sedimentation showed that fold geometries change between the single models (Figs. 7 and 8). Fig. 7 documents the

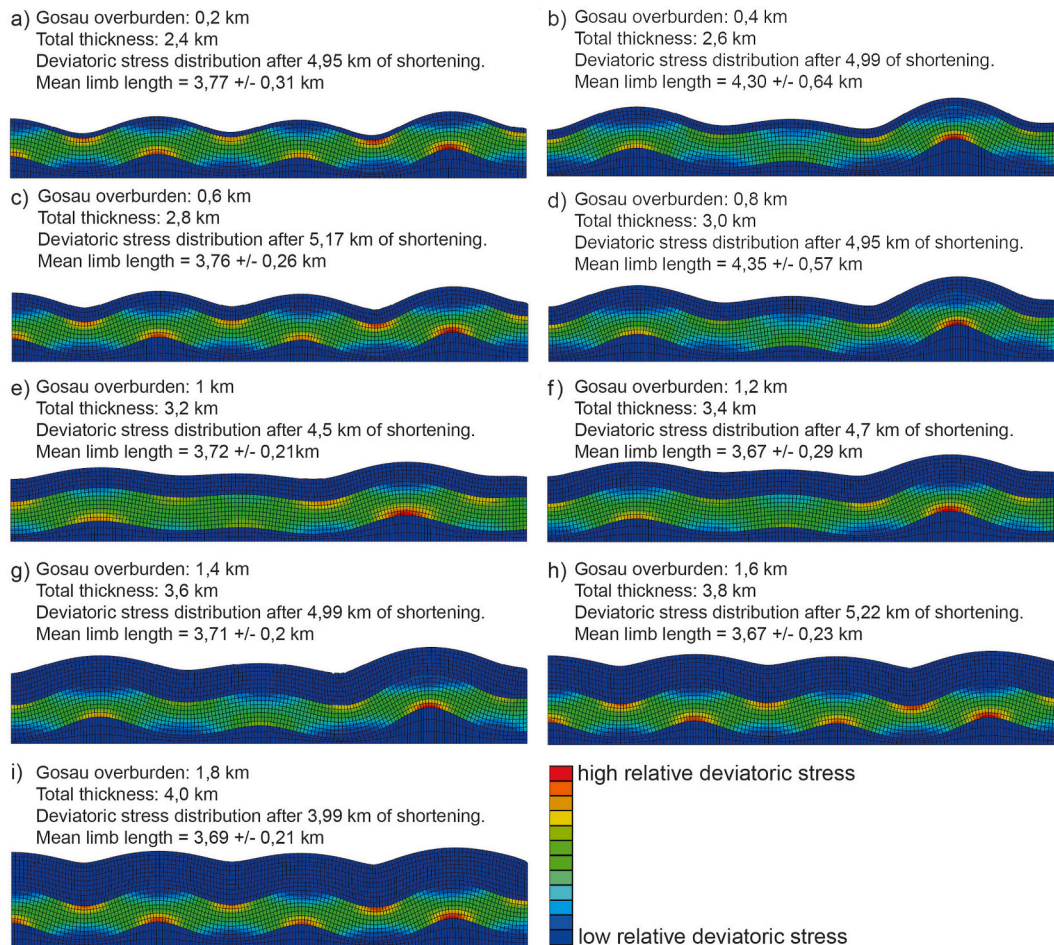


Fig. 8. Results from modelling folding with increasing overburden. The material model is linear elasticity. Coloration represents the relative deviatoric stress distribution. The intermediate competent unit and the basal incompetent unit have constant thickness in the models, while the top incompetent unit ("Gosau overburden") increases in thickness. Material parameters: Layer 1 (bottom): E-Module 2 000 000 kN/m², Poisson ratio 0.25; Layer 2 (middle): E-Module 80 000 000 kN/m², Poisson ratio 0.2; Layer 3: E-Module 10 000 000 kN/m²; Poisson ratio 0.25.

influence of erosion on the development of folds. With increasing erosion, the number of folds increases while the limb lengths of the folds decrease. Two anticlines develop without erosion, or eroding only 0.2 km (Fig. 7a and b, respectively). Between 0.4 km and 1.2 km of erosion (Fig. 7c–i) three anticlines develop. The model of Fig. 7i (1.6 km of erosion) is an exception and most probably due to numerical issues, as it has the least shortening and only two anticlines are visible in this fold train. The other models all show similar shortening length, the small deviation in length are due to incrementation steps (length of deformation applied in each substep). In the models of Fig. 7j–l four anticlines are developed. Thus, as result of this modelling approach it can be shown that qualitatively the number of anticlines, which is connected to the limb length of folds, increases with the decreasing thickness of the competent layer.

The model series depicted in Fig. 8a–i tests the influence of a growing overburden on folding. The thickness of layers 1 and 2 in the last erosion model (Fig. 7l) were used in the re-sedimentation models, and an increasing thickness of layer 3 b between 0.2 km and 1.8 km. Overburden and horizontal stresses are recalculated for each setting. From the start, the model series of Fig. 8a–i has a very regular fold pattern with three or four anticlines.

3.1. Analysing folds – numeric results and field example

A simple way to describe buckle folds is the determination of limb lengths (e.g., Biot, 1961; Ramberg, 1960; Ramsay and Huber, 1987). Buckle folds develop an initial arc length at the beginning of buckling which remains constant during ongoing shortening. The limb length of a fold represents half of the arc length. During the model runs, we observed that the number of folds is stable, and the limb lengths in the models depend on the number of folds.

Fold limb lengths were measured along a path drawn in the middle of the competent layer (Fig. 9). All limb lengths were measured and plotted (Fig. 10 and Fig. 11). Some folds end against the model margin, therefore some limbs are significantly shorter than the majority of limbs (see Figs. 7 and 8). These outliers were not included in the calculation of mean values and standard deviations. In some models we observed two hierarchies of folds (a to e and i to k of Fig. 7), and two anticlines and a syncline arch upward in a larger anticlinorium (“irregular fold geometries”). We still calculated a mean value from the smaller limb lengths, having in mind that the results might be biased.

3.1.1. Measured limb length from numeric results

The measured limb lengths from the erosion model (Fig. 7) are summarised in Fig. 10. Layer 1 is of constant thickness whereas layer 2 and 3a are stepwise eroded. The limb length varies around the value of 4–5.5 km. Limb lengths decrease in the models with decreasing thickness of layer 3a, but increases in the models where the thickness of the competent layer decreases to a maximum of 5.5 km. When the thickness of the model is about 2.6 km (Layer 2 eroded down to 2 km instead of 3 km at the beginning), the limb length gets shorter and varies around 3.3–3.7 km. The standard deviations are larger when the fold geometry is irregular. There is no simple relationship between the thickness of the

model or the competent layer and limb length.

The results of limb length measurements for the models of re-sedimentation are shown in Fig. 11. The competent layer 2 has a constant thickness of 1,6 km while the thickness of the incompetent layer 3 b increases. The limb length does not vary systematically, and the mean values from the individual experiments scatter between 3.7 and 4.1 km. It is very likely that this is a result of combination of stiffness ratio and layer thickness.

3.1.2. Limb lengths from field data and numeric model (Fig. 12)

To compare the model results with field examples, limb lengths from the cross sections of the Karwendel Mountains were measured along the median line of the competent layer from the base of the Anisian limestones to the erosive top of the Norian platform (Fig. 5). We plotted the limb lengths both against the thickness of the competent layer 2 (Fig. 12a) and against total model thickness (Fig. 12b). To be able to plot total thickness from field data we used the pre-deformational thickness of the incompetent layer 1 from area balancing (Fig. 5c), and for the Bettelwurf anticline of Fig. 5a the observed 300 m thickness (see chapter 2.1.1). Because no synorogenic sediments occur in the study area, only results from the erosion model were used for comparison.

All measured limb lengths of Fig. 12 are shorter than their model counterparts with comparable total or competent layer thickness. Neither the modelled nor the measured limb lengths have a simple, i.e., linear relationship to competent layer thickness or total model thickness. Numeric results from the model vary between 3.2 and 5.5 km. The limb lengths measured in the cross sections range between 2.7 and 4.7 km.

4. Discussion

The numeric model aimed to test if buckle folding is a possible deformation process for the Karwendel thrust sheet in the western NCA. As in many previously studied cases (e.g., Humair et al., 2020; Ruh et al., 2012; Simpson, 2009; Yamato et al., 2011), the numeric model showed that buckle folding is only possible if there is a very weak layer at the base (décollement) and the rheology contrast between the competent layer and the incompetent base layer is high. Therefore, both field evidence (Fig. 5) and the numeric model described are not in conflict with an interpretation of the km-scale folds above the Karwendel thrust as buckle folds, developed above the very weak décollement horizon of the salt bearing Permian to Triassic evaporites (Haselgebirge and Reichenthal Fm.).

4.1. Erosion and sedimentation

Further, we aimed to test the influence of erosion and sedimentation on the development of buckle folds. The numeric model is insensitive to dynamic changes during erosion or sedimentation. A decreasing thickness of the competent layer in successive models causes increasing limb lengths, until a threshold is reached. Beyond this threshold limb lengths jump to a smaller value, and then increase again (Fig. 7e–l, Fig. 10). An incompetent overburden on top of a thin competent layer had minor

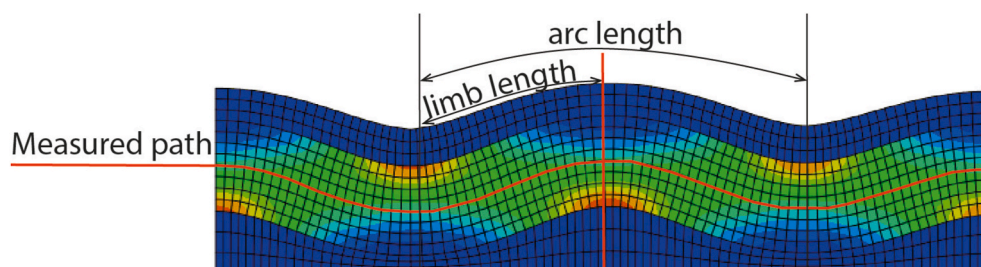


Fig. 9. Measured line, arc length and limb length of the folds.

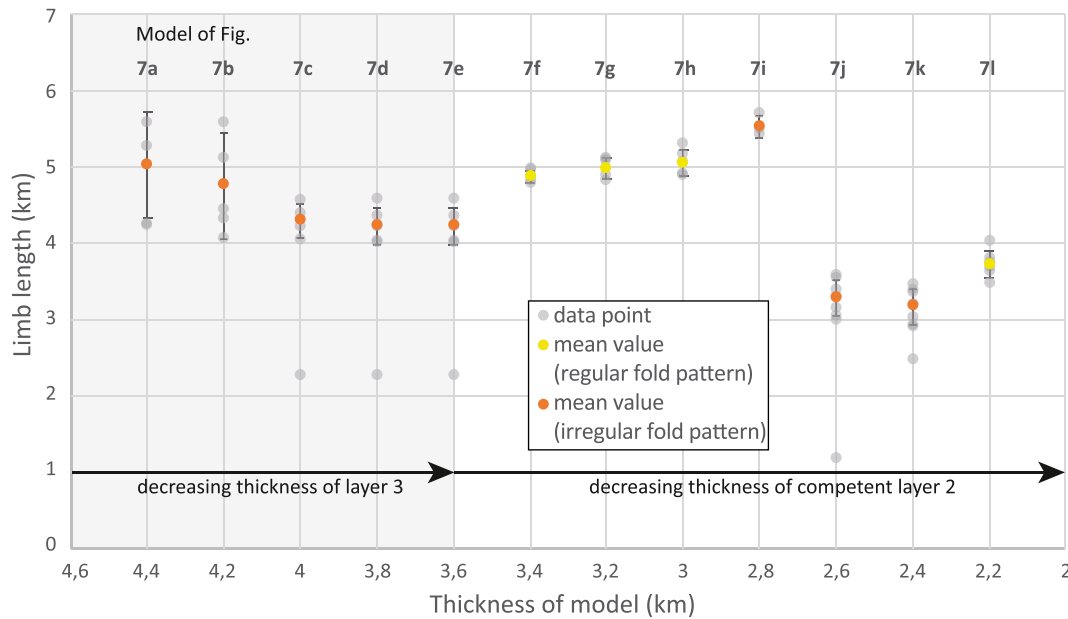


Fig. 10. Calculated limb lengths from the numeric model of erosion, mean values (orange and yellow) and standard deviation. The mean values of irregular fold geometries are coloured in orange. (For interpretation of the references to colour in this figure legend, the reader is referred to the Web version of this article.)

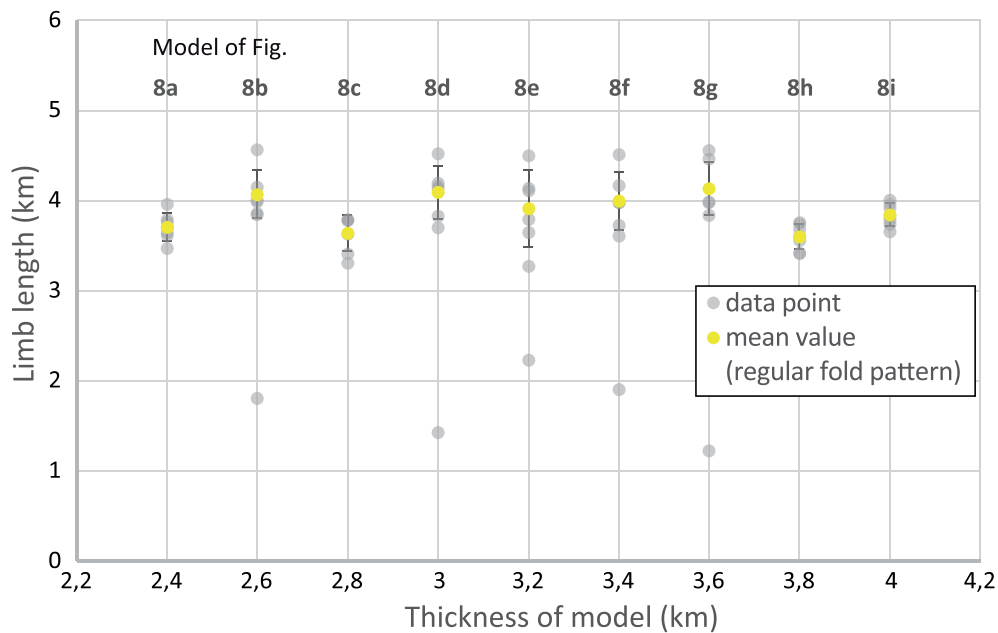


Fig. 11. Calculated limb lengths from the numeric model of re-sedimentation, mean values (orange and yellow) and their standard deviation. Irregular fold geometries are coloured in orange. (For interpretation of the references to colour in this figure legend, the reader is referred to the Web version of this article.)

effects on the developing limb lengths, whatever the thickness of the overburden was (Fig. 11), however, in experiments with overburden on a thick competent layer, limb length decreases with decreasing overburden (Fig. (Fig. 7a – e, Fig. 10). This effect decreases with decreasing thickness of the overburden (Fig. 7c – e, Fig. 10).

This is in line with analytical models (e.g., Biot, 1961; Ramberg, 1960; Ramsay and Huber, 1987; Schmalholz et al., 2002) that showed that limb lengths of buckle folds are dependent on the thickness of the competent layer. However, the complex behaviour of the model tested here demonstrates that more parameters influence the fold nucleation process, as rheology contrast, and thickness ratio of décollement versus competent layer.

The erosion experiments demonstrated that limb lengths comparable

to the fold limbs observed in the field only form after a part of the competent layer 2 is eroded. The comparison with limb lengths measured in the cross sections of Fig. 5 showed that there is, for some data, a severe misfit as compared to the numeric results (Fig. 12). This misfit probably relates to some assumptions during modelling, that are discussed below. Here we evaluate the measured data and qualitatively discuss their relationship to the modelled values:

- (1) The thickness of the incompetent layer 1 is known (see chapter 2.1.1). Considering more thickness in layer 1 would shift the data points of Fig. 12b to the right, but not in Fig. 12a, therefore it is rather the thickness of the competent layer that was underestimated. This thickness is not known everywhere. It is definitely

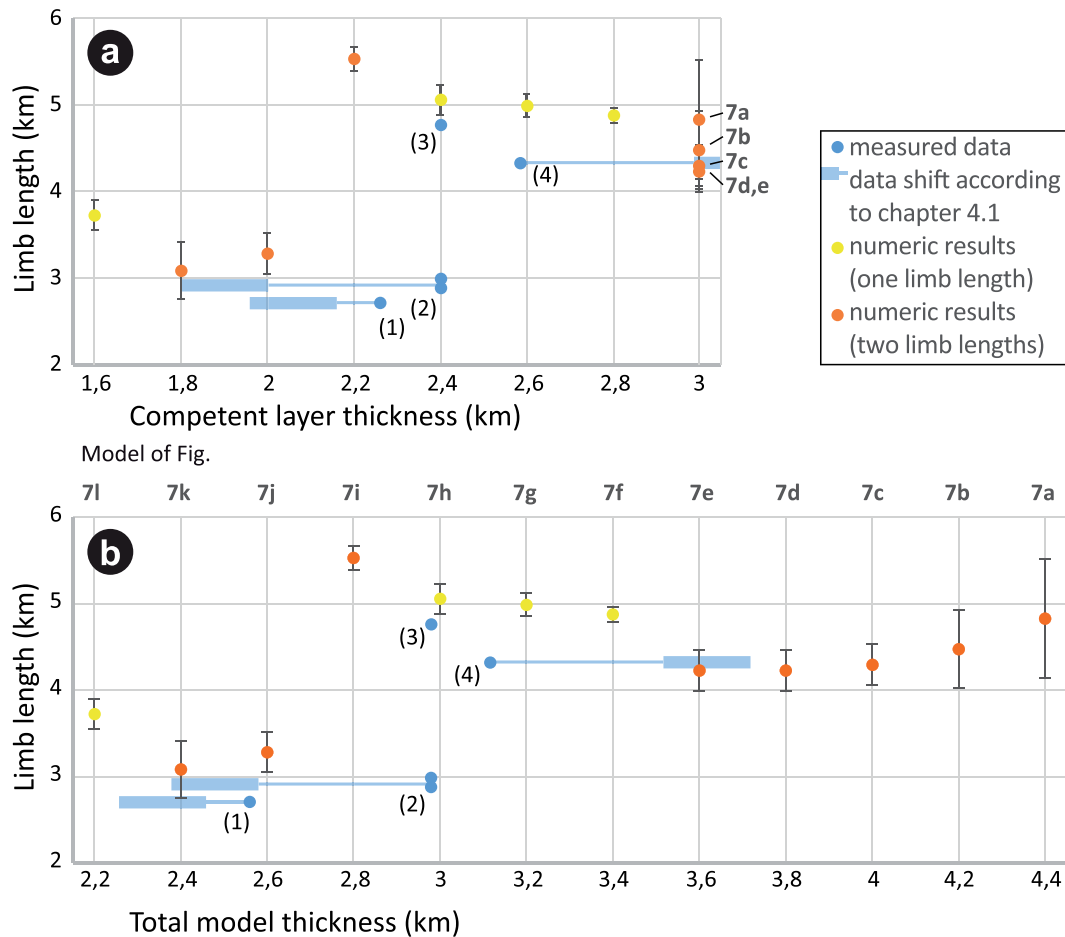


Fig. 12. Comparison of modelled limb lengths versus limb lengths measured in the cross sections of Fig. 5. Modelled and measured limb lengths plotted against (a) thickness of the competent layer, and (b) plotted against total model thickness. Measured total thickness is the thickness of the competent layer 2 plus the thickness of the incompetent layer 1 derived from area-balancing (see chapter 2.1.1 and Fig. 5c). The diagrams of (a) and (b) show competent above total thickness of Fig. 7e - l, except for models a - d. (1) = southern limb of Bettelwurf anticline of Fig. 5a and (2) and = southern and northern limb of Solstein anticline of Fig. 5b and (3) = southern limb of Bettelwurf anticline and (4) = southern limb of Larchetkar anticline of Fig. 5b.

not a solution for data points 1 and 2 of Fig. 12, that have a competent layer thickness larger than modelled folds with comparable limb length.

- (2) When measuring competent layer thickness in the cross sections, we implicitly assume that no erosion after folding has occurred. This assumption is incorrect, as significant Quaternary erosion affected the Alps (e.g., Hinderer, 2001; van Husen, 2000). While the southern limb of the Bettelwurf anticline (Fig. 5b) has a limb length close to the modelled values (3 of Fig. 12), the southern limb of the Larchetkar anticline (Fig. 5b) has a much larger misfit (4 of Fig. 12). It must be kept in mind that competent layer thickness is controlled by cross section construction below the Larchetkar anticline, as it cannot be directly measured, the cross section could easily be changed to fit the modelled data. If we speculate, that the measured, present-day competent layer thickness is correct, which is supported by the layer-cake geometry of the restored section of Fig. 5c, an additional thickness of 400–600 m present at the time of fold nucleation would increase competent layer thickness and bring the data point close to the modelled values (Fig. 12). This additional thickness would have been eroded since onset of folding.
- (3) The modelling assumes constant erosion across the model. The most conspicuous data are the limb lengths of the Solstein anticline (2 of Fig. 12), where competent layer thickness is well controlled (Fig. 5b). Competent layer thickness is larger than in

modelled folds having comparable competent layer thickness. Removal of 400–600 m thickness in the competent layer would suffice to bring the data close to the modelled values, however, competent layer thickness was measured in the northern limb of the Solstein anticline. Therefore, removal of a northward tapering wedge of rock prior to nucleation of the Solstein anticline (cf Fig. 5c) could possibly solve the problem. The same may be true for the southern limb of the Bettelwurf anticline (Figs. 5a and 1 of Fig. 12), however less erosion (100–300 m) would be necessary in this case.

The comparison of measured and modelled competent layer thicknesses leads to the conclusion, that layer thickness should be measured directly in the fold, that is compared to the modelling results, and that post-folding erosion needs to be taken into account.

The competent layer thicknesses prior to folding in accordance with modelled fold limb lengths are shown in Fig. 5c and have been drawn in the position of the fold axial planes. Thickness measured close to the cores of synclines are well in accordance with modelled limb length whereas thickness is under- or overestimated in the anticlines. All data together define an erosion surface dipping to the south with respect to bedding, however, if the surface is regarded to be horizontal during formation, bedding would have been slightly tilted to the north.

Whatever the age of the synorogenic sediments in the Karwendel mountains is, Late Cretaceous or Late Paleogene (Fig. 4; see chapters 1.2

and 1.3), they were deposited on top of an unconformity formed prior to folding. This unconformity cuts deeper into the sedimentary succession toward the south (Fig. 5c), and this can be extended to the north to the Karwendel syncline, where Lower Cretaceous sediments are preserved in the Karwendel thrust sheet (Figs. 4 and 5a). Eroding more than 2 km rocks on top of a contracting orogenic wedge (nappe stacking started in the Lower Cretaceous) will probably cause thickening in that area, to preserve taper of the wedge. It is well possible that antiformal stacking within the Tannheim thrust sheet and related out-of-sequence thrusting (Fig. 1b) are a consequence of this erosion.

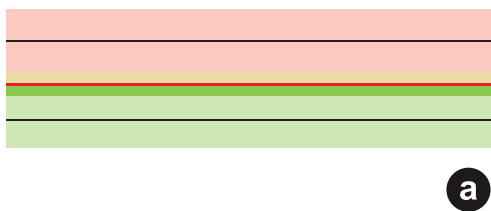
The effects of erosion and sedimentation in fold- and-thrust belts detached above a weak basal layer were also discussed in other numeric experiments (e.g., Collignon et al., 2014; Heydarzadeh et al., 2020; Najafi et al., 2020; Simpson, 2006; Yamato et al., 2011). For example, Collignon et al. (2014) showed that erosion and sedimentation do have a minor effect on fold wavelengths (arc lengths) but enhance the amplification of anticlines by loading synclines with syntectonic deposits. However, regional erosion or deposition prior to the start of fold growth determines some boundary conditions of folding and thus the developing fold geometries, as demonstrated in this study.

Erosion after fold nucleation might have favoured the amplification of already existing anticlines in the Karwendel mountains. However, no new folds formed significantly later, as (1) there was no unfolded unit left, (2) the axis orientation of km-scale folds cannot be changed during subsequent deformation. Newly formed Neogene folds should have NW-trending axes, and such folds were only observed on the small scale close to out-of-sequence thrusts (Kilian and Ortner, 2019).

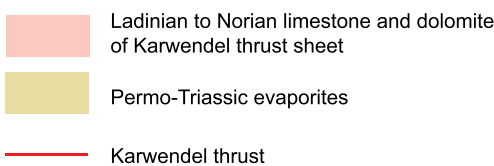
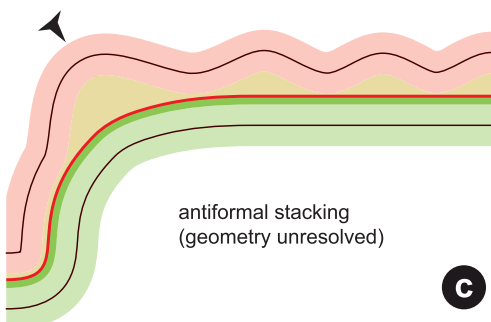
4.2. Kinematic evolution

Kilian and Ortner (2019) concluded that the Karwendel thrust sheet arrived of today's Karwendel mountains on top of a salt pillow, that allowed transport without folding. The redistribution of the salt along the décollement allowed folding on top of the décollement to start. Structural data suggested that folding significantly post-dated initial stacking of thrust sheets in the late Early Cretaceous. The numeric results allow a further interpretation. Limb lengths as observed in the field only develop after a decrease in lithostatic pressure related to Upper Cretaceous and/or Paleogene erosion. As shortening continued after initial emplacement of thrust sheets folding probably initiated in the late

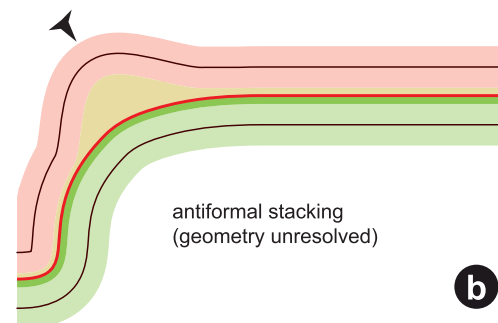
Emplacement of the Karwendel thrust sheet on top of the Haselgebirge décollement. Erosion increasing to the south removed part of Ladinian to Norian of Karwendel thrust sheet (not shown)



The locked décollement causes folding to migrate into the hinterland, creating buckle folds on top of the evaporitic décollement



Antiformal stacking within the Tannheim thrust sheet causes folding of the Karwendel thrust. Evaporites migrate into the fold core and cause fold amplification in the Karwendel thrust sheet. The frontal part is mechanically coupled (pin)



Ongoing shortening. The lock is broken by an out-of-sequence long-limb thrust, that uses a décollement in Rhätian marls.

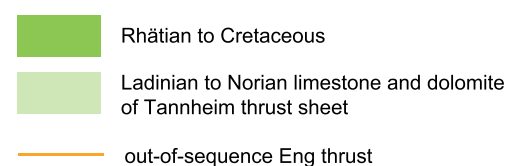
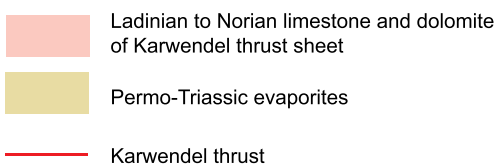
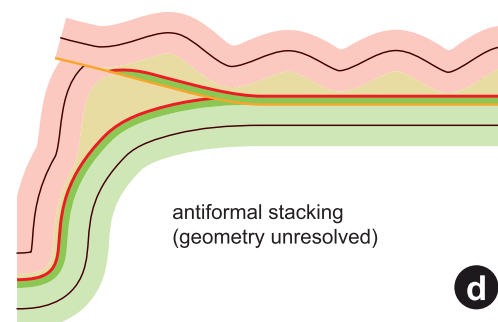


Fig. 13. Simplified kinematic development of the structures observed. (a) Stacking of thrust sheets in the late Lower Cretaceous along the detachment horizon (Permian to Triassic evaporites). (b) Folding of the thrust as a consequence of antiformal stacking in the lower, Tannheim thrust sheet, migration of evaporites into the fold core and amplification of the anticline within the upper, Karwendel thrust sheet during Paleogene shortening. Folding of the thrust locks the detachment (pin). (c) Buckling within the Karwendel thrust sheet in the hinterland of the fold locking the detachment. (d) Further Oligo-Miocene shortening causes out-of-sequence thrusting that breaks the lock and cuts across the fold locking the detachment. The out-of-sequence thrust uses a structurally deeper décollement in Rhätian marls. Further explanations in main text.

Upper Cretaceous to Paleogene (as fold axes indicate, see Fig. 5).

The results of the numeric model gave a contribution to the development of structures in the hanging wall of the Karwendel thrust. We observed two kinds of folds in the Karwendel Mountains: (1) Folds above the thrust plane and (2) folds folding hanging wall and footwall together. All folds nucleated during Paleogene N- to NNE-directed transport (see Fig. 5). The numeric model dealt only with the folds above the Karwendel thrust, which developed as buckle folds above the very weak décollement horizon of the salt bearing Permian to Triassic evaporites (Haselgebirge and Reichenhall Fm.). Folds refolding hanging wall and footwall are not related to the weak décollement at the base of the Karwendel thrust sheets, but to a structurally deeper one within or at the base of the Tannheim thrust sheet (cf. Fig. 1b).

In Fig. 13 we sketched a possible development of the structures observed in the field (cross sections Fig. 5a) based on the structural investigations of Kilian and Ortner (2019) and the numeric results presented here.

Based on fold axis orientations, the buckle folds within the Karwendel thrust sheet and the fold deforming hanging wall and footwall together developed contemporaneously and have parallel fold axis trends (Fig. 5). However, kinematically it is required that the Karwendel thrust is folded first, and the anticline on top of the thrust is amplified by migration of evaporites into its core (Fig. 13b). Folding of the thrust is most probably related to thickening of the underlying Tannheim thrust sheet by antiformal stacking of slices (see Fig. 1b). The fold in the Karwendel thrust locks it, and subsequent shortening causes buckling of within the Karwendel thrust sheet, as it is “buttressed” against the locked zone (Fig. 13c). Shortening continues into the Oligocene to Miocene (Kilian and Ortner, 2019), and the structurally deeper out-of-sequence Eng and Bäralpl thrusts (Figs. 4 and 5) develop, that follow a décollement within the Rhätian Kössen marls in the uppermost part of the Tannheim thrust sheet (Fig. 13d). Therefore, the décollement along the Permian to Triassic evaporites along the Karwendel thrust was no longer weak. Salt expulsion might have strengthened the thrust itself, and forced the décollement into the footwall.

A problem in the kinematic evolution is the long-time span between Lower Cretaceous stacking of thrust sheets (Fig. 13a), and folding interpreted to have Paleogene age (Fig. 13b and c). This interpretation is based on the comparison of fold axis trends with transport directions as reported in previous studies (e.g., Eisbacher and Brandner, 1996; Kilian and Ortner, 2019; Ortner, 2003b), and to plate convergence vectors (e.g., Dewey et al., 1989; Handy et al., 2010; Le Breton et al., 2021). If the Karwendel folds had Paleogene age, shortening between the Early Cretaceous and Paleogene would have left no trace in this part of the NCA, in spite of well-documented shortening elsewhere (Ortner, 2001; Ortner et al., 2016). In the Late Cretaceous, the NCA thrust belt was transported across tectonically deeper Penninic units and should have experienced shortening. If, however, the Karwendel folds have a Late Cretaceous age, fold axis orientation must be controlled by, e.g., differential transport as suggested for oblique folds in the Pyrenees (Muñoz et al., 2013; Pueyo et al., 2002), or strain partitioning across strike slip faults (Allen et al., 2001; Jones and Tanner, 1995), which has been suggested in the Mieming mountains west of the study area (MM of Fig. 1; Ortner and Bitterlich, 2016). In such a case, the unconformity reconstructed here would be the regional unconformity found at the base of the Upper Cretaceous synorogenic deposits of the NCA.

4.3. Modelling

The results obtained in this study show that simple numerical models allow a qualitative interpretation of folding processes in geological units in dependence of differences in rheology and layer thickness. However, this approach does not allow an evaluation of stresses. Working with a multi-layer approach could bring new insights into the deformation behaviour and would be closer to the “real” stratigraphic succession in the study area. Other numeric models, e.g., from the Zagros Mountains

(Yamato et al., 2011), showed that multiple weak layers intensify the fold growth in comparison to thrusting. To be able to evaluate stresses and consequently also faulting more complex rheology has to be used.

5. Conclusion

Although a numeric model is a strong simplification of reality, the model gave a new perspective on interpreting structures in the Karwendel Mountains. Km-scale folds in the hanging wall of the Karwendel thrust can be interpreted as buckle folds, developed after the emplacement of the Karwendel thrust sheet and after partial erosion of the latter.

Our modelling demonstrated some key requirements of buckle folding: (1) The existence of a very incompetent décollement, which lies in the salt-bearing evaporitic Haselgebirge-Reichenhall horizon at the base of the Karwendel thrust sheet, and (2) major erosion prior to folding, as the full, up to 5 km thick sedimentary succession cannot be folded with limb lengths comparable to those observed in the field. Only the reduction of the competent carbonate platforms to roughly half of their original thickness facilitates folding with limb lengths around 3–4 km as observed in cross sections. This erosion does not only control fold limb lengths, but also the overall kinematic evolution in the area.

This study also emphasises the need for geometric-rheological models for the construction of cross sections in salt-detached fold-and-thrust belts. Material characteristics strongly influence the geometry of structures, still many cross sections are entirely drawn by using geometric models.

Author statement

During preparation of the manuscript „Buckle folding in the Northern Calcareous Alps - field observations and numeric experiments“ the contribution of the authors were:

Sinah Kilian wrote the original draft of the manuscript. She did the numerical modelling, and mapped part of the study area. Thus, both modelling and structural analysis are based on Sinah's work, which was part of her PhD thesis.

Hugo Ortner was the main supervisor of Sinah Kilian's PhD thesis. He developed the idea, contributed field data, and helped revising the manuscript.

Barbara Schneider-Muntau was a supervisor of Sinah Kilian's PhD thesis. She introduced Sinah Kilian to numerical modelling, and helped revising the manuscript.

Declaration of competing interest

The authors declare that they have no known competing financial interests or personal relationships that could have appeared to influence the work reported in this paper.

Acknowledgments

The Tiroler Wissenschaftsfonds and the Doctoral program of the University of Innsbruck supported this research. We thank Petroleum Experts Ltd who provided the Move software package free of charge in the frame of their academic software initiative. Move was used to draw the cross sections of Fig. 5. The constructive reviews of O. Fernandez and S. Schmalholz improved this contribution significantly and are greatly acknowledged.

References

- Abbassi, M.R., Mancktelow, N.S., 1992. Single layer buckle folding in non-linear materials—I. Experimental study of fold development from an isolated initial perturbation. *J. Struct. Geol.* 14, 85–104.
- Allen, M.B., Alsop, G.I., Zhemchuzhnikov, V.G., 2001. Dome and basin refolding and transpressive inversion along the Karatau Fault System, southern Kazakhstan. *J. Geol. Soc.* 158, 83.

- Amperfer, O., 1902. Bericht über die Neuaufnahme des Karwendelgebirges. Verh. Geol. Bundesanst. 274–276, 1902.
- Amperfer, O., 1914. Besprechung mit O. Schlagintweit, K. Ch. v. Loesch und H. Mylius über das Wettersteingebirge. Verhandlungen der k.k. Geologischen Reichsanstalt 1914, 338–352.
- Auer, M., Eisbacher, G.H., 2003. Deep structure and kinematics of the Northern Calcareous Alps (TRANSALP profile). *Int. J. Earth Sci.* 92, 210–227.
- Bachmann, G.H., Müller, M., 1981. Geologie der Tiefbohrung Vorderriß 1 (Kalkalpen, Bayern). *Geol. Bavarica* 81, 17–53.
- Barani, O., 2012. The effect of lower detachment zone on buckle folds Geometry. *Journal of Structural Engineering and Geotechnics* 2, 43–47.
- Bechstäd, T., Mostler, H., 1976. Riff-Becken-Entwicklung in der Mitteltrias der westlichen nördlichen Kalkalpen. *Zeitschr. Dt. Geol. Ges.* 127, 271–289.
- Behrmann, J.H., Tanner, D.C., 2006. Structural Synthesis of the Northern Calcareous Alps. *TRANSALP segment, Tectonophysics*, pp. 225–240.
- Biot, M.A., 1961. Theory of folding of stratified viscoelastic media and its implications in tectonics and orogenesis. *Geol. Soc. Am. Bull.* 72, 1595–1620.
- Biot, M.A., Taylor, G.I., 1957. Folding instability of a layered viscoelastic medium under compression. *Proc. Roy. Soc. Lond. Math. Phys. Sci.* 242, 444–454.
- Brandner, R., Poleschinski, W., 1986. Stratigraphie und Tektonik am Kalkalpensüdrand zwischen Zirl und Seefeld in Tirol. *Jahresberichte und Mitteilungen des Oberrheinischen Geologischen Vereines. Neue Folge* 68, 67–92.
- Butler, R.W.H., Bond, C.E., Cooper, M.A., Watkins, H., 2020. Fold-thrust structures – where have all the buckles gone? *Geological Society, London, Special Publications* 487, 21–44.
- Collignon, M., Kaus, B.J.P., May, D.A., Fernandez, N., 2014. Influences of surface processes on fold growth during 3-D detachment folding. *G-cubed* 15, 3281–3303.
- Currie, J.B., Patnode, H.W., Trump, R.P., 1962. Development of folds in sedimentary strata. *Geol. Soc. Am. Bull.* 73, 655–673.
- Czech, J., Huber, H., 1990. Gesteinskennwerte aus Laborversuchen. *Befbau* 8, 129–133.
- Davis, D.M., Engelder, T., 1985. The role of salt in fold-and-thrust belts. *Tectonophysics* 119, 67–88.
- Dewey, J.F., Helman, M.L., Turco, E., Hutton, D.H.W., Knott, S.D., 1989. Kinematics of the western mediterranean. In: Coward, M.P., Dietrich, D., Park, R.G. (Eds.), *Alpine Tectonics*. Geological Society, London, pp. 265–283.
- Diersche, V., 1980. Die Radiolarite des Oberjura im Mittelabschnitt der Nördlichen Kalkalpen. *Geotekt. Forsch.* 58, 217.
- Donofrio, D.A., Brandner, R., Poleschinski, W., 2003. Conodonten der Seefeld-Formation: ein Beitrag zur Bio- und Lithostratigraphie der Hauptdolomit-Plattform (Obertrias, westliche Nördliche Kalkalpen, Tirol). *Geol. - Palaeontol. Mitteil. Innsbr.* 26, 91–107.
- Donofrio, D.A., Heissel, G., Mostler, H., 1980. Beiträge zur Kenntnis der Partnachschichten (Trias) des Tor- und Rontales und zum Problem der Abgrenzung der Lechtaldecke im Nordkarwendel. *Mitt. Österr. Geol. Ges.* 73, 55–94.
- Eberli, G.P., 1988. The evolution of the southern continental margin of the Jurassic tethys ocean as recorded in the Allgäu Formation of the Austroalpine nappes of Graubünden (Switzerland). *Eclogae Geol. Helv.* 81, 175–214.
- Eckert, A., Connolly, P., Liu, X., 2014. Large-scale mechanical buckle fold development and the initiation of tensile fractures. *G-cubed* 15, 4570–4587.
- Eisbacher, G.H., Brandner, R., 1996. Superposed fold thrust structures and high angle faults, northwestern Calcareous Alps, Austria. *Eclogae Geol. Helv.* 89, 553–571.
- Eisbacher, G.H., Linzer, G.-H., Meier, L., 1990. A depth extrapolated structural transect across the Northern Calcareous Alps of western Tirol. *Eclogae Geol. Helv.* 83, 711–725.
- Faupl, P., Pöber, E., Wagreich, M., 1987. Facies development of the Gosau group of the eastern parts of the Eastern Alps. In: Flügel, H.W., Faupl, P. (Eds.), *Geodynamics of the Eastern Alps. Deuticke, Wien*, pp. 142–154.
- Fernandez, N., Kaus, B.J.P., 2014. Influence of pre-existing salt diapirs on 3D folding patterns. *Tectonophysics* 637, 354–369.
- Fernández, O., Habermüller, M., Grasmann, B., 2020. Hooked on salt: rethinking Alpine tectonics in Hallstatt (Eastern Alps, Austria). *Geology* 49, 325–329.
- Frehner, M., 2011. The neutral lines in buckle folds. *J. Struct. Geol.* 33, 1501–1508.
- Freudenberger, W., Schwed, K., 1996. Erläuterungen zur geologischen Karte von Bayern 1:500 000. Bayerisches Geologisches Landesamt, München.
- Frisch, J., 1975. Sedimentologische, lithofazielle und paläogeographische Untersuchungen in den Reichenhaller Schichten und im Alpinen Muschelkalk der Nördlichen Kalkalpen zwischen Lech und Isar. *Jb. Geol. Bundesanst.* 118, 75–117.
- Frisch, W., Kuhlemann, J., Dunkl, L., Szekeley, B., 2001. The Dachstein Paleosurface - a mosaic stone in the geomorphological evolution of the Alps. *Int. J. Earth Sci.* 90, 500–518.
- Froitzheim, N., Schmid, S., Conti, P., 1994. Repeated change from crustal shortening to orogen parallel extension in the Austroalpine units of Graubünden. *Eclogae Geol. Helv.* 87, 559–612.
- Fruth, I., Scherreihs, R., 1982. Hauptdolomit (norian), stratigraphy, paleogeography and diagenesis. *Sediment. Geol.* 32, 195–231.
- Gaupp, R., 1982. Sedimentationsgeschichte der kalkalpinen Mittelkreide (Allgäu, Tirol, Vorarlberg). *Zitteliana* 8, 33–72.
- Ghassemi, M.R., Schmalholz, S.M., Ghassemi, A.R., 2010. Kinematics of constant arc length folding for different fold shapes. *J. Struct. Geol.* 32, 755–765.
- Goff, D.F., Wiltshcko, D.V., Fletcher, R.C., 1996. Décollement folding as a mechanism for thrust-ramp spacing. *J. Geophys. Res.: Solid Earth* 101, 11341–11352.
- Goffey, G., Craig, J., Needham, T., Scott, R.E., 2010. Hydrocarbons in Contractual Belts. Geological Society, London.
- Golebiowski, R., 1991. Becken und Riffe der alpinen Obertrias - lithostratigraphie und Biofazies der Kössener Formation. In: Nagel, D., Rabeder, G. (Eds.), *Exkursionen im Jungpaläozoikum und Mesozoikum Österreichs*. Österreichische Paläontologische Gesellschaft, Wien, pp. 79–119.
- Granado, P., Roca, E., Strauss, P., Pelz, K., Muñoz, J.A., 2018. Structural styles in fold-and-thrust belts involving early salt structures: the Northern Calcareous Alps (Austria). *Geology* 47, 51–54.
- Guest, B., Guest, A., Axen, G., 2007. Late Tertiary tectonic evolution of northern Iran: a case for simple crustal folding. *Global Planet. Change* 58, 435–453.
- Haas, J., Kovács, S., Krystyn, L., Lein, R., 1995. Significance of Triassic facies zones in terrane reconstructions in the Alpine-North Pannonian domain. *Tectonophysics* 242, 19–40.
- Handy, M.R., Schmid, S.M., Bousquet, R., Kissling, E., Bernoulli, D., 2010. Reconciling plate-tectonic reconstructions of Alpine Tethys with the geological-geophysical record of spreading and subduction in the Alps. *Earth Sci. Rev.* 102, 121–158.
- Heißel, G., 1978. Karwendel - geologischer Bau und Versuch einer tektonischen Rückformung. *Geol. - Palaeontol. Mitteil. Innsbr.* 8, 227–288.
- Heydarzadeh, K., Ruh, J.B., Vergés, J., Hajjilibeigi, H., Gharabegli, G., 2020. Evolution of a structural basin: numerical modelling applied to the dehdasht basin, central Zagros, Iran. *J. Asian Earth Sci.* 187, 104088.
- Hinderer, M., 2001. Late Quaternary denudation of the Alps, valley and lake fillings and modern river loads. *Geodin. Acta* 14, 231–263.
- Huang, K.-P., Chang, K.-J., Wang, T.-T., Jeng, F.-S., 2010. Buckling folds of a single layer embedded in matrix – folding behavior revealed by numerical analysis. *J. Struct. Geol.* 32, 960–974.
- Hudleston, P.J., Holst, T.B., 1984. Strain analysis and fold shape in a limestone layer and implications for layer rheology. *Tectonophysics* 106, 321–347.
- Humair, F., Bauville, A., Epard, J.-L., Schmalholz, S.M., 2020. Interaction of folding and thrusting during fold-and-thrust-belt evolution: insights from numerical simulations and application to the Swiss Jura and the Canadian Foothills. *Tectonophysics* 789, 228474.
- Jackson, M.P.A., Hudec, M.R., 2017. *Salt Tectonics - Principles and Practice*. Cambridge University Press, Cambridge.
- Jacobshagen, V., 1965. Die Allgäuschichten (Jura-Fleckenmergel) zwischen Wettersteingebirge und Rhein. *Jb. Geol. Bundesanst.* 108, 1–114.
- Jamison, W.R., 1987. Geometric analysis of fold development in overthrust terranes. *J. Struct. Geol.* 9, 207–219.
- Jeng, F.S., Huang, K.P., 2008. Buckling folds of a single layer embedded in matrix – theoretical solutions and characteristics. *J. Struct. Geol.* 30, 633–648.
- Jeng, F.S., Lin, M.L., Lai, Y.C., Teng, M.H., 2002. Influence of strain rate on buckle folding of an elasto-viscous single layer. *J. Struct. Geol.* 24, 501–516.
- Jerz, H., 1966. Untersuchungen über Stoffbestand, Bildungsbedingungen und Paläogeographie der Raibler Schichten zwischen Lech und Inn (Nördl. Kalkalpen). *Geol. Bavarica* 56, 3–100.
- Johnson, A.M., Fletcher, R.C., 1994. *Folding of Viscous Layers*. Columbia University Press, New York.
- Jones, R.R., Tanner, P.W.G., 1995. Strain partitioning in transpression zones. *J. Struct. Geol.* 17, 793–802.
- Kilian, S., Ortner, H., 2019. Structural evidence of in-sequence and out-of-sequence thrusting in the Karwendel mountains and the tectonic subdivision of the western Northern Calcareous Alps. *Austrian Journal of Earth Sciences* 112, 62–83.
- Krois, P., Stingl, V., 1994. Kretazische "Augensteine"? - Notiz zu einem fraglichen Gosauvorkommen im Karwendel (Tirol, Österreich). *Jb. Geol. Bundesanst.* 137, 289–293.
- Lacombe, O., Lavé, J., Roure, F., Vergés, J., 2007. *Thrust Belts and Foreland Basins - from Fold Kinematics to Hydrocarbon Systems*. Springer, Berlin.
- Lan, L., Hudleston, P.J., 1991. Finite-element models of buckle folds in non-linear materials. *Tectonophysics* 199, 1–12.
- Le Breton, E., Brune, S., Ustaszewski, K., Zahirovic, S., Seton, M., Müller, R.D., 2021. Kinematics and extent of the piemont-liguria basin – implications for subduction processes in the Alps. *Solid Earth* 12, 885–913.
- Lein, R., 1987. Evolution of the Northern Calcareous Alps during Triassic times. In: Flügel, H.W., Faupl, P. (Eds.), *Geodynamics of the Eastern Alps. Deuticke, Wien*, pp. 85–102.
- Leitner, C., Spötl, C., 2017. Chapter 21 - the eastern Alps: multistage development of extremely deformed evaporites. In: Soto, J.I., Flinch, J.F., Tari, G. (Eds.), *Permo-Triassic Salt Provinces of Europe, North Africa and the Atlantic Margins*. Elsevier, Amsterdam, pp. 467–482.
- Li, S., 2013. *Numerical Studies of the Deformation of Salt Bodies with Embedded Carbonate Stringers*. PhD thesis. RWTH, Aachen, p. 281.
- Linzer, H.-G., Ratschbacher, L., Frisch, W., 1995. Transpressional collision structures in the upper crust: the fold thrust belt of the Northern Calcareous Alps. *Tectonophysics* 242, 41–61.
- Liu, X., Eckert, A., Connolly, P., 2016. Stress evolution during 3D single-layer visco-elastic buckle folding: implications for the initiation of fractures. *Tectonophysics* 679, 140–155.
- Llorens, M.-G., Bons, P.D., Griera, A., Gomez-Rivas, E., Evans, L.A., 2013. Single layer folding in simple shear. *J. Struct. Geol.* 50, 209–220.
- Mancktelow, N.S., 1999. Finite-element modelling of single-layer folding in elasto-viscous materials: the effect of initial perturbation geometry. *J. Struct. Geol.* 21, 161–177.
- Mattern, F., Wang, P., 2008. Out-of-sequence thrusts and paleogeography of the rhodanubian Flysch belt (eastern Alps) revisited. *Int. Jour. Earth Sci.* 97, 821–833.
- Miller, H., 1963. Der Bau des westlichen Wettersteingebirges. *Zeitschr. Dt. Geol. Ges.* 113, 409–425.
- Miller, H., 1965. Die Mitteltrias der Mieminger Berge mit Vergleichen zum westlichen Wettersteingebirge. *Verh. Geol. Bundesanst.* 187–212, 1965.

- Mitra, S., 2002. Structural models of faulted detachment folds. *AAPG Bull.* 86, 1673–1694.
- Moullas, E., Schmalholz, S.M., 2020. The importance of interfacial instability for viscous folding in mechanically heterogeneous layers. In: Bond, C.E., Lebit, H.D. (Eds.), *Folding and Fracturing of Rocks*. Geological Society, London, pp. 45–58.
- Müller-Jungbluth, W.-U., 1971. Sedimentologische Untersuchungen des Hauptdolomits der östlichen Lechtaler Alpen, Tirol. In: Mostler, H. (Ed.), *Beiträge zur Mikrofazies und Stratigraphie von Tirol und Vorarlberg*, Festband des Geol. Inst., 300-Jahr-Feier. Univ. Innsbruck, Innsbruck, pp. 255–308.
- Muñoz, J.-A., Beamud, E., Fernández, O., Arbués, P., Dinarès-Turell, J., Poblet, J., 2013. The Ainsa Fold and thrust oblique zone of the central Pyrenees: kinematics of a curved contractional system from paleomagnetic and structural data. *Tectonics* 32, 1142–1175.
- Nagel, K.H., Schütz, K.I., Schütz, S., Wilmers, W., Zeil, W., 1976. Die geodynamische Entwicklung der Thiersee- und Karwendelmulde (Nördliche Kalkalpen). *Geol. Rundsch.* 65, 536–557.
- Najafi, M., Beamud, E., Ruh, J., Mouthereau, F., Tahmasbi, A., Bernaola, G., Yassaghi, A., Motamedi, H., Sherkati, S., Hassan Goodarzi, M.G., Vergés, J., 2020. Pliocene growth of the dowlatabad syncline in frontal fars arc: folding propagation across the Zagros fold belt, Iran. *GSA Bulletin* 1–23.
- Nemcok, M., Schamel, S., Gayer, R., 2005. Thrust Belts - Structural Architecture, Thermal Regimes, and Petroleum Systems. Cambridge University Press, Cambridge.
- Nilfouroushan, F., Pysklywec, R., Cruden, A., Koyi, H., 2013. Thermal-mechanical modeling of salt-based mountain belts with pre-existing basement faults: application to the Zagros fold and thrust belt, southwest Iran. *Tectonics* 32, 1212–1226.
- Nittel, P., 2006. Beiträge zur Stratigraphie und Mikropaläontologie der Mitteltrias der Innsbrucker Nordkette (Nördliche Kalkalpen, Austria). *GeoAlp* 3, 93–145.
- Ortner, H., 2001. Growing folds and sedimentation of the Gosau Group, Muttekopf, Northern Calcareous Alps, Austria. *Int. J. Earth Sci.* 90, 727–739.
- Ortner, H., 2003a. Cretaceous thrusting in the western part of the Northern Calcareous Alps (Austria) - evidences from synorogenic sedimentation and structural data. *Mitt. Österr. Geol. Ges.* 94, 63–77.
- Ortner, H., 2003b. Local and far field stress – analysis of brittle deformation in the western part of the Northern Calcareous Alps, Austria. *Geol. - Palaontol. Mittl. Innsbr.* 26, 109–131.
- Ortner, H., 2015. Fernerkundung mit Hilfe von Orthofotos und Geländemodellen in der Geologie – Beispiele aus den Nördlichen Kalkalpen. *GeoAlp* 11, 5–27, 2014.
- Ortner, H., 2016. Field Trip 4: deep water sedimentation on top of a growing orogenic wedge - interaction of thrusting, erosion and deposition in the Cretaceous Northern Calcareous Alps. *GeoAlp* 13, 141–182.
- Ortner, H., Aichholzer, S., Zerlauth, M., Pilsner, R., Fügenschuh, B., 2015. Geometry, amount and sequence of thrusting in the subalpine Molasse of western Austria and southern Germany, European Alps. *Tectonics* 34, 1–30.
- Ortner, H., Bitterlich, L., 2016. The zugsitzige cross section and the structure of the northern calcareous Alps. In: Ortner, H. (Ed.), *Abstract Volume of GeoTiro12016 - Annual Meeting of DGGV and PANGEA Austria*. Institute of Geology, University of Innsbruck, Innsbruck, p. 248.
- Ortner, H., Gaupp, R., 2007. Synorogenic sediments of the western northern calcareous Alps. *GeoAlp* 4, 133–148.
- Ortner, H., Kositz, A., Willingshofer, E., Sokoutis, D., 2016. Geometry of growth strata in a transpressive fold belt in field and analogue model: Gosau Group at Muttekopf, Northern Calcareous Alps, Austria. *Basin Res.* 28, 731–751.
- Ortner, H., Reiter, F., Brandner, R., 2006. Kinematics of the Inntal shear zone-sub-Tauern ramp fault system and the interpretation of the TRANSALP seismic section, Eastern Alps, Austria. *Tectonophysics* 414, 241–258.
- Ortner, H., Stingl, V., 2001. Facies and basin development of the Oligocene in the lower Inn valley, Tyrol/Bavaria. In: Piller, W., Rasser, M. (Eds.), *Paleogene in Austria*. Österreichische Akademie der Wissenschaften, Wien, pp. 153–196.
- Palotai, M., Pálfi, J., Sasvári, Á., 2017. Structural complexity at and around the Triassic-Jurassic GSSP at Kuhjoch, Northern Calcareous Alps, Austria. *Int. J. Earth Sci.* 106, 2475–2487.
- Peresson, H., Decker, K., 1997. The Tertiary dynamics of the northern Eastern Alps (Austria): changing palaeostresses in a collisional plate boundary. *Tectonophysics* 272, 125–157.
- Pfiffner, O.A., 1993. The structure of the Helvetic nappes and its relation to mechanical stratigraphy. *J. Struct. Geol.* 511–521.
- Poblet, J., Muñoz, J., Trave, A., Serra - Kiel, J., 1998. Quantifying the kinematics of detachment faults using three-dimensional geometry: application to the Mediano anticline (Pyrenees, Spain). *Geol. Soc. Am. Bull.* 110, 111–125.
- Price, N.J., Cosgrove, J.W., 1990. *Analysis of Geological Structures*. Cambridge University Press, Cambridge.
- Pueyo, E.L., Millán, H., Poció, A., 2002. Rotation velocity of a thrust: a paleomagnetic study in the external sierras (southern Pyrenees). *Sediment. Geol.* 146, 191–208.
- Ramberg, H., 1960. Relationships between length of arc and thickness of pygmatically folded veins. *Am. J. Sci.* 258, 36–46.
- Ramberg, H., 1963. Fluid dynamics of viscous buckling applicable to folding of layered rocks. *AAPG Bull.* 47, 484–505.
- Ramsay, J.G., Huber, M.I., 1987. *The Techniques of Modern Structural Geology*, vol. 2. Folds and Fractures. Academic Press, London.
- Rowan, M.G., Kligfield, R., 1992. Kinematics of large-scale asymmetric buckle folds in overthrust shear: an example from the Helvetic nappes. In: McClay, K.R. (Ed.), *Thrust Tectonics*. Chapman & Hall, London, pp. 165–173.
- Rüffer, T., Zamperelli, V., 1997. Facies and biota of Anisian to Carnian carbonate platforms in the Northern Calcareous Alps (Tyrol and Bavaria). *Facies* 37, 115–136.
- Ruh, J.B., Kaus, B.J.P., Burg, J.-P., 2012. Numerical investigation of deformation mechanics in fold-and-thrust belts: influence of rheology of single and multiple décollements. *Tectonics* 31.
- Sanders, D., 1998. Tectonically controlled late cretaceous terrestrial to neritic sedimentation, Gosau group, Northern Calcareous Alps (Tyrol, Austria). *Facies* 39, 139–178.
- Sanders, D., Höfling, R., 2000. Carbonate deposition in mixed siliciclastic-carbonate environments on top of an orogenic wedge (Late Cretaceous, Northern Calcareous Alps, Austria). *Sediment. Geol.* 137, 127–146.
- Sarnthein, M., 1965. Sedimentologische Profilreihen aus den mitteltriadischen Karbonatgesteinen der Kalkalpen nördlich und südlich von Innsbruck. *Verh. Geol. Bundesanst.* 119–162, 1965.
- Sarnthein, M., 1967. Versuch einer Rekonstruktion der mitteltriadischen Paläogeographie um Innsbruck. Österreich. *Geol. Rundsch.* 56, 116–127.
- Schauberger, O., 1986. Bau und Bildung der Salzlagerstätten des ostalpinen Salinars. *Arch. Lagerstättenforsch. Geol. Bundesanst.* 7, 217–254.
- Schmalholz, S.M., Mancktelow, N.S., 2016. Folding and necking across the scales: a review of theoretical and experimental results and their applications. *Solid Earth* 7, 1417–1465.
- Schmalholz, S.M., Podladchikov, Y.Y., 2001. Strain and competence contrast estimation from fold shape. *Tectonophysics* 340, 195–213.
- Schmalholz, S.M., Podladchikov, Y.Y., Burg, J.P., 2002. Control of folding by gravity and matrix thickness: implications for large-scale folding. *J. Geophys. Res.: Solid Earth* 107, ETG 1-1-ETG 1-16.
- Schmalholz, S.M., Schmid, D.W., 2012. Folding in power-law viscous multi-layers. *Phil. Trans. Math. Phys. Eng. Sci.* 370, 1798–1826.
- Schmid, S.M., Fügenschuh, B., Kissling, E., Schuster, R., 2004. Tectonic map and overall architecture of the Alpine orogen. *Eclogae Geol. Helv.* 97, 93–117.
- Schmidegg, O., 1951. Die Stellung der Haller Salzlagerstätte im Bau des Karwendelgebirges. *Jb. Geol. Bundesanst.* 94, 159–205.
- Sherwin, J.-A., Chapple, W.M., 1968. Wavelengths of single-layer folds; a comparison between theory and observation. *Am. J. Sci.* 266, 167.
- Simpson, G., 2006. Influence of erosion and deposition on deformation in fold belts. In: Willett, S.D., Hovius, N., Brandon, M.T., Fisher, D.M. (Eds.), *Tectonics, Climate, and Landscape Evolution*. Geological Society of America, pp. 267–281.
- Simpson, G.D.H., 2009. Mechanical modelling of folding versus faulting in brittle-ductile wedges. *J. Struct. Geol.* 31, 369–381.
- Spötl, C., 1989. Die Salzlagerstätte von Hall in Tirol - ein Überblick über den Stand der geologischen Erforschung des 700jährigen Bergbaubetriebes. *Veröff. Mus. Ferdinandeum* 69, 137–167.
- Stampfli, G.M., Mosar, J., Marquer, R., Marchant, R., Baudin, T., Borel, G., 1998. Subduction and obduction processes in the Swiss Alps. *Tectonophysics* 296, 159–204.
- Strauss, P., Granado, P., Muñoz, J.A., 2021. Subsidence analysis of salt tectonics-driven carbonate minibasins (Northern Calcareous Alps, Austria). *Basin Res.* 33, 968–990.
- Stüwe, K., Schuster, R., 2010. Initiation of subduction in the Alps: continent or ocean? *Geology* 38, 175–178.
- Suppe, J., 1983. Geometry and kinematics of fault-bend folding. *Am. J. Sci.* 283, 684–721.
- Tollmann, A., 1976a. *Analyse des klassischen nordalpinen Mesozoikums*. Deuticke, Wien.
- Tollmann, A., 1976b. *Der Bau der Nördlichen Kalkalpen*. Deuticke, Wien.
- van Husen, D., 2000. Geological processes during the quaternary. *Mitt. Österr. Geol. Ges.* 92, 135–156.
- Vergés, J., 2012. Multiple detachment folding in Pusht-e Kuh arc, Zagros: role of mechanical stratigraphy. In: McClay, K., Shaw, J.H., Suppé, J. (Eds.), *Thrust Fault-Related Folding*, Tulsa, pp. 69–94.
- von Soos, P., Engel, J., 2008. *Eigenschaften von Boden und Fels - ihre Ermittlung im Labor*. In: Witt, K.J. (Ed.), *Grundbau-Taschenbuch*. Ernst & Sohn, Berlin, pp. 123–218.
- Wagreich, M., Decker, K., 2001. Sedimentary tectonics and subsidence modelling of the type Upper Cretaceous Gosau basin (Northern Calcareous Alps, Austria). *Int. J. Earth Sci.* 90, 714–726.
- Wagreich, M., Faupl, P., 1994. Paleogeography and geodynamic evolution of the Gosau Group of the Northern Calcareous Alps (Late Cretaceous, Eastern Alps, Austria). *Paleogeogr. Paleoclimatol. Paleoecol.* 110, 235–254.
- Yamato, P., Kaus, B.J.P., Mouthereau, F., Castellort, S., 2011. Dynamic constraints on the crustal-scale rheology of the Zagros fold belt, Iran. *Geology* 39, 815–818.